

Final Report

5 December 1974 — 17 December 1975

ANALYTICS OF CRYSTAL GROWTH IN SPACE

by

Chong E. Chang

Robert A. Lefever

William R. Wilcox

Distribution of this report is provided in the interest
of information exchange. Responsibility for the

contents resides with the authors.

(NASA-CR-144214) ANALYTICS OF CRYSTAL
GROWTH IN SPACE Final Report, 5 Dec. 1974 -
17 Dec. 1975 (University of Southern Calif.)
74 p HC \$4.50

N76-19978

CSCL 20B

Unclas

G3/76

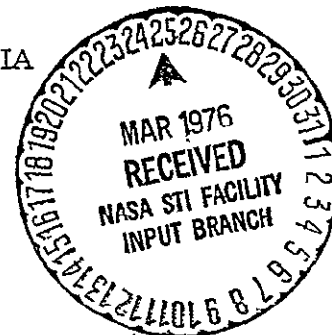
20647

Prepared under Contract No. NAS8-29847

UNIVERSITY OF SOUTHERN CALIFORNIA

Chemical Engineering Department

Los Angeles, California 90007



For

NASA — GEORGE C. MARSHALL SPACE FLIGHT CENTER

ANALYTICS OF CRYSTAL GROWTH IN SPACE

by

Chong E. Chang, Robert A. Lefever, and William R. Wilcox

University of Southern California
Los Angeles, California 90007

ABSTRACT

The variation of radial impurity distribution induced by surface tension driven flow increases as the zone length decreases in silicon crystals grown by floating zone melting. In combined buoyancy driven and surface tension driven convection at the gravity of earth, the buoyancy contribution becomes relatively smaller as the zone diameter decreases and eventually convection is dominated by the surface tension driven flow (in the case of silicon, for zones of less than about 0.8 cm in diameter). Preliminary calculations for sapphire suggest the presence of an oscillatory surface tension driven convection as a result of an unstable melt surface temperature that results when the zone is heated by a radiation heater.

TABLE OF CONTENTS

	page
Abstract	ii
List of Illustrations	iv
List of Tables	vii
Summary	1
I. INTRODUCTION	3
II. NUMERICAL ACCURACY AND CONVERGENCE TEST	4
A. Convergence Test	4
B. Grid Refinement Test	5
C. Discussion	11
III. INFLUENCE OF THE ZONE LENGTH ON IMPURITY SEGREGATION	12
IV. COMBINED SURFACE TENSION DRIVEN AND BUOYANCY DRIVEN CONVECTION	13
A. Model for Analysis of the Combined Convection	23
B. Influence of the Zone Length	24
C. Influence of the Zone Diameter	24
V. FLOATING ZONE MELTING OF SAPPHIRE AT ZERO G	40
A. Computations with Free Parameters	40
B. Survey of the Physical Properties of Sapphire	43
C. Computations with Electron Beam Heating	45
D. Computations with Radiation Heating	48
E. Oscillatory Convection with Radiation Heating	51
1) Equations for Transient Convection	51
2) Numerical Computations	53
VI. PROPOSED ADDITIONAL STUDIES	61
References	62
Appendix A	63

LIST OF ILLUSTRATIONS

	page
Figure 1. Isotherms and streamlines for $M'=350$, $a=0.5$ cm, and $Pr=0.023$, with electron beam heating and 21×41 grid	6
Figure 2. Concentration field for 5 cm/hr zone travel rate, $Sc=5.0$, $k_0=0.1$, $M'=350$, and $Pr=0.023$	7
Figure 3. Axial concentration profiles at three radial positions for zone travel rates of 1 and 5 cm/hr	8
Figure 4. Streamlines for $M'=350$ and $a=0.5$ cm with parabolic temperature profile along melt surface	14
Figure 5. Concentration field for $M'=350$, $a=0.5$ cm, and zone travel rate of 5 cm/hr	15
Figure 6. Isotherms and streamlines for $M'=350$, $a=0.5$ cm, and $Pr=0.023$, with electron beam heating	16
Figure 7. Concentration field for conditions as in Fig. 6, with $Sc=5$ and $k_0=0.1$	17
Figure 8. Streamlines for $M'=350$ and $a=0.5$ cm, with parabolic temperature profile along the melt surface	18
Figure 9. Concentration field for conditions as in Fig. 7, with $Sc=5$ and $k_0=0.1$	19
Figure 10. Isotherms and streamlines for $M'=350$, $a=0.5$ cm and $Pr=0.023$, with electron beam heating	20
Figure 11. Concentration field for conditions as in Fig. 10, with $Sc=5$ and $k_0=0.1$	21
Figure 12. Impurity concentration profiles in resulting crystals	22
Figure 13. Isotherms and streamlines for $M'=350$, $a=1$ cm, $Pr=0.023$, and $Gr_h=77.5$	25

	page
Figure 14. Isotherms and streamlines for $M'=350$, $a=1$ cm, $Pr=0.023$, and $Gr_h=1240$	26
Figure 15. Isotherms and streamlines for $M'=350$, $a=0.1$ cm, $Pr=0.023$, and $Gr_h=3.1$ with electron beam heating	29
Figure 16. Isotherms and streamlines for $a=0.25$ cm and $Gr_h=19.4$	30
Figure 17. Isotherms and streamlines for $a=1$ cm and $Gr_h=310$	31
Figure 18. Isotherms and streamlines for $a=2$ cm and $Gr_h=1240$	32
Figure 19. Isotherms and streamlines for $a=3$ cm and $Gr_h=2790$	33
Figure 20. Isotherms and streamlines for $a=4$ cm and $Gr_h=4960$	34
Figure 21. Nusselt numbers for combined surface tension driven and buoyancy driven flow versus zone diameter	35
Figure 22. Streamlines for $M'=350$, $a=2$ cm, and $Gr_h=0$, with parabolic temperature pro- file along the melt surface	37
Figure 23. Isotherms and streamlines for $M'=350$, $a=2$ cm, $Pr=0.023$, and $Gr_h=0$, with electron beam heating	38
Figure 24. Maximum stream function versus M' at zero g	39
Figure 25. Nusselt numbers versus Gr_h/M'^2 at 1 g	41
Figure 26. The influence of the Grashof number on the axial flow component	42
Figure 27. Isotherms and streamlines for $a=0.5$ cm and free parameters such as $M'=$ 22 and $Pr=0.34$, with electron beam heating	44

Figure 28. Conduction isotherms for electron beam heating of sapphire with radiation to the surroundings at 2033°C	page 46
Figure 29. Conduction isotherms for electron beam heating of sapphire with radiation to the surroundings at 2010°C	47
Figure 30. Isotherms and streamlines for electron beam heating of sapphire with $a = 0.5$ cm, $M' = 35$, and $Pr = 12$	49
Figure 31. Isotherms and streamlines for electron beam heating of sapphire with $a = 0.5$ cm, $M' = 140$, and $Pr = 12$	50
Figure 32. Conduction isotherms for radiation heating of sapphire	52
Figure 33. Isotherms and streamlines for radiation heating of sapphire with $M' = 585$, $Pr = 12$, and $a = 0.5$ cm at $\tau = 0$	55
Figure 34. Isotherms and streamlines at $\tau = 0.0786$	56
Figure 35. Isotherms and streamlines at $\tau = 0.1572$	57
Figure 36. Isotherms and streamlines at $\tau = 0.2358$	58
Figure 37. Isotherms and streamlines at $\tau = 0.3144$	59
Figure 38. Temperature oscillation at free melt surface of sapphire	60

LIST OF TABLES

	page
Table I. Summary of the surface tension driven convection in floating zone melting with various operating conditions	9
Table II. Ratio of Nusselt numbers at 1g and 0g for various experimental conditions	28

SUMMARY

This report is supplementary to the 1974 Annual Report [1] on the analysis of surface tension driven convection in floating zone melting. The detailed mathematical development and numerical method used for calculation of the momentum, heat and mass transfer equations are reported in Reference [1], and are omitted in this report.

The influence of the operating parameters such as zone geometry, heating methods (electron beam or radiation heating) and gravity of earth are investigated. We have attempted to solve transient equations for floating zone melting of sapphire for a possible oscillatory convection with radiation heating. The following conclusions are made from the results of our computer calculations for silicon, except where noted:

- 1) Radial distribution of impurity in the crystal increases as the zone length decreases due to the fact that there is less convection at the center of the short zone.
- 2) As the zone size (length and/or diameter) decreases, the buoyancy effect due to the earth's gravity diminishes and convection is dominated by the surface tension induced flow.
- 3) The floating zones of high Prantl number materials (for example, sapphire) are susceptible to an oscillatory convection due to the unstable temperature at the free melt surface when a radiation heater is employed.

- 4) The surface tension driven convection tends to be more well defined with electron beam heating (i. e., concentrated heat supply) than with radiation heating (i. e., distributed heat supply).
- 5) The maximum stream function of pure surface tension driven flow increases as surface tension parameter M' increases with the relationship of $\psi_{\max} = 0.199 (M')^{0.6}$.
- 6) The buoyancy effect is relatively small near the free melt surface and large near the center of the zone for combined surface tension driven and buoyancy driven flows.

During the year, three papers were published [2-4] and a fourth was accepted for publication [5]. A paper was presented at the Stanford Conference on Crystal Growth in July [6] and a paper on related studies was presented at the Pasadena meeting of the American Physical Society in December [7].

I. INTRODUCTION

As reported in the 1974 Annual Report [1], numerical analysis of convection in floating zone melting of silicon has shown that the surface tension driven convection is vigorous.

During the current contract period (January 1975 to December 1975), the influence of both operating parameters and property parameters on surface tension driven convection were investigated.

The following operative parameters were considered:

- 1) Zone geometry, such as aspect ratio and zone diameter.
- 2) Relative importance of buoyancy driven convection due to the gravity of earth.
- 3) Heating modes, including electron beam heating and radiation heating.

In addition to silicon, sapphire was selected to investigate the influence of physical properties on the surface tension driven flow.

On earth, the relative importance of the buoyancy effect is expected to increase as zone size increases, since the volume of the melt increases at a greater rate than the free melt surface area. This argument was applied to a small zone, in which the surface tension driven flow is expected to be predominant due to the large free melt surface area relative to the melt volume. From the partial differential equation for the momentum transfer, a parameter combining the Grashof number (Gr_h) and the dimensionless surface tension parameter (M') were derived in order to define the relative importance in the combined buoyancy driven and the surface tension driven flow.

The floating zones of high Prandtl number materials, such as organic compounds and metal oxides, are more susceptible to oscillatory convection when radiation heating is used, since the heat radiated on the free melt surface from the heater tends to accumulate as the melt moves along the surface due to the low heat conduction rate from the surface into the bulk melt. A transient solution of the transport equations will be necessary to further investigate the possibility of surface tension driven oscillatory convection in the floating zone melting of sapphire.

II. NUMERICAL ACCURACY AND CONVERGENCE TEST

The accuracy and convergence in the previous numerical solutions of the surface tension driven flow in floating zone melting were examined for a representative case as follows:

1) The same number of grid points were used, but a higher number of iterations was made by placing a more stringent accuracy limit. The results were compared with the previous results in order to verify the convergence.

2) The grid size was reduced and the computation was carried out for a representative case with a sufficient number of iterations.

A. Convergence Test

Convergence tests were made by increasing the number of iterations until no appreciable difference was found in the solution of the test problem. Iteration was terminated when the difference between the current value of stream function, $\psi_{i,j}^{(s+1)}$ at the $(s+1)^{\text{th}}$ iteration

and the old value of stream function $\psi_{i,j}^{(s)}$ at the $(s)^{th}$ iteration passed the accuracy limit at every grid point. We tested the case shown in Figure 7 in the First Annual Report [1] where the accuracy limit was

$$|\psi_{i,j}^{(s+1)} - \psi_{i,j}^{(s)}| < 0.005$$

under which the required number of iterations was 217. When the accuracy limit of 0.001 instead of 0.005 was used, the required number of iterations was 383. However, there was no essential difference in the pattern of stream functions, the fact of which indicates a sufficient convergence in this problem.

B. Grid Refinement Test

The stream functions, temperature and concentration fields shown in the previous figures (Figures 7 and 18, Ref. [1]) were tested as a representative case by refining the grid size from 11×21 to 21×41 grid points and comparing them. An accuracy limit of 0.0005 was employed for the stream function. The computation of stream function was terminated after about 2100 iterations. The results in stream functions, temperature and concentration fields with 21×41 grid points are shown in Figures 1 through 3. In Table I, the stream functions, vorticity and fluid velocities are compared with the results computed with 11×21 grid points. The numerical value of the stream function showed about 1% deviation near the free melt surface where the convection is weakest. However, there was no essential difference in the pattern of the isotherms and the streamlines, nor in the intensity of the flow, as shown in Figure 1. The

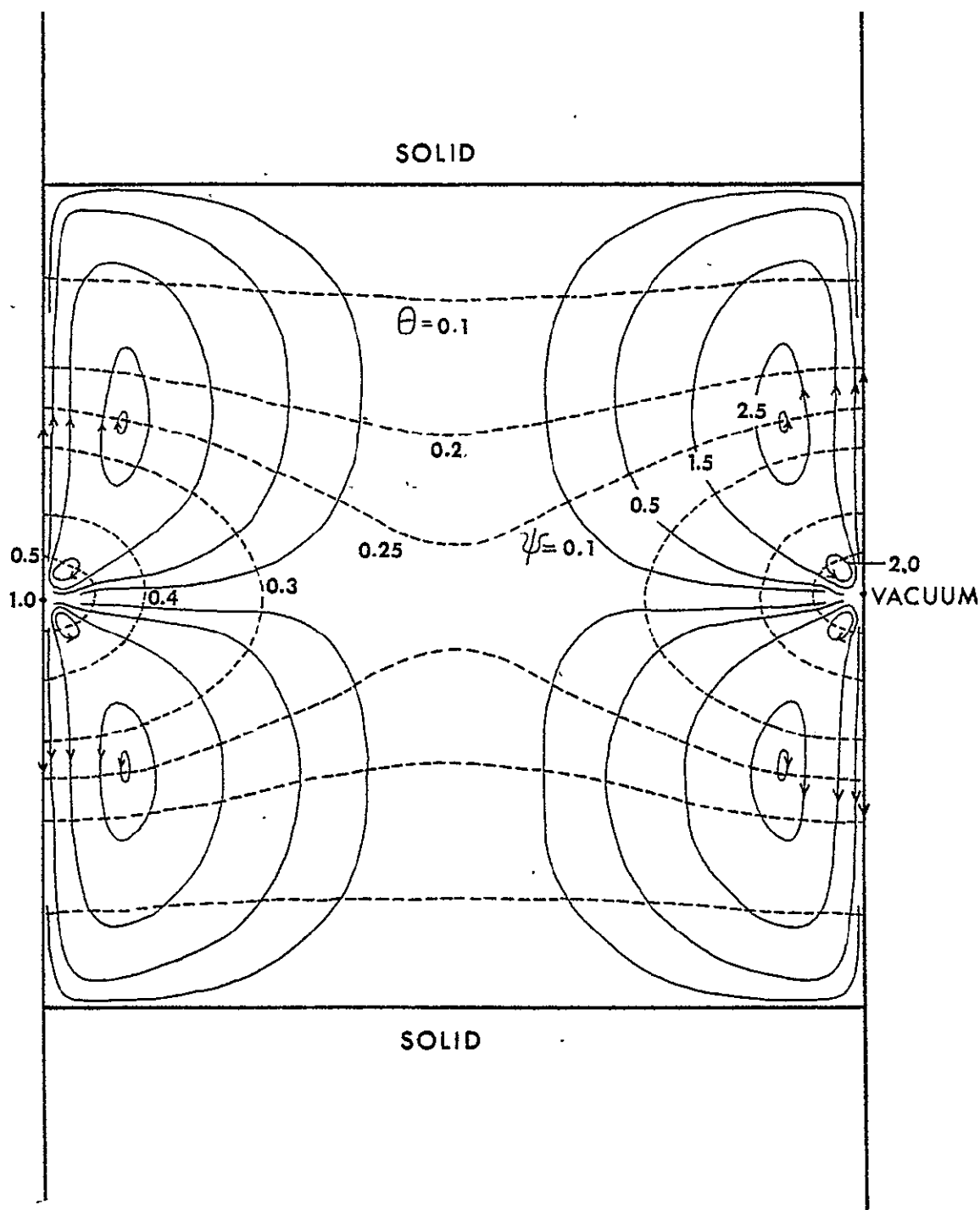


Figure 1. Computer calculated isotherms θ (dotted lines) and streamlines ψ (solid lines) for surface tension driven flow in floating zone melting at zero gravity, using the computed temperature fields for electron beam heating of silicon with $(T_o - T_b) = 0.05^\circ\text{C}$, $T_o = T_b$, $\delta_s = 0.3$, $a = 0.5$ cm, $M' = 350$, $Pr = 0.023$, $v_c = 5$ cm/hr, and $\theta = (T - T_b)/(T_o - T_b)$. Calculations performed with 21×41 grid.

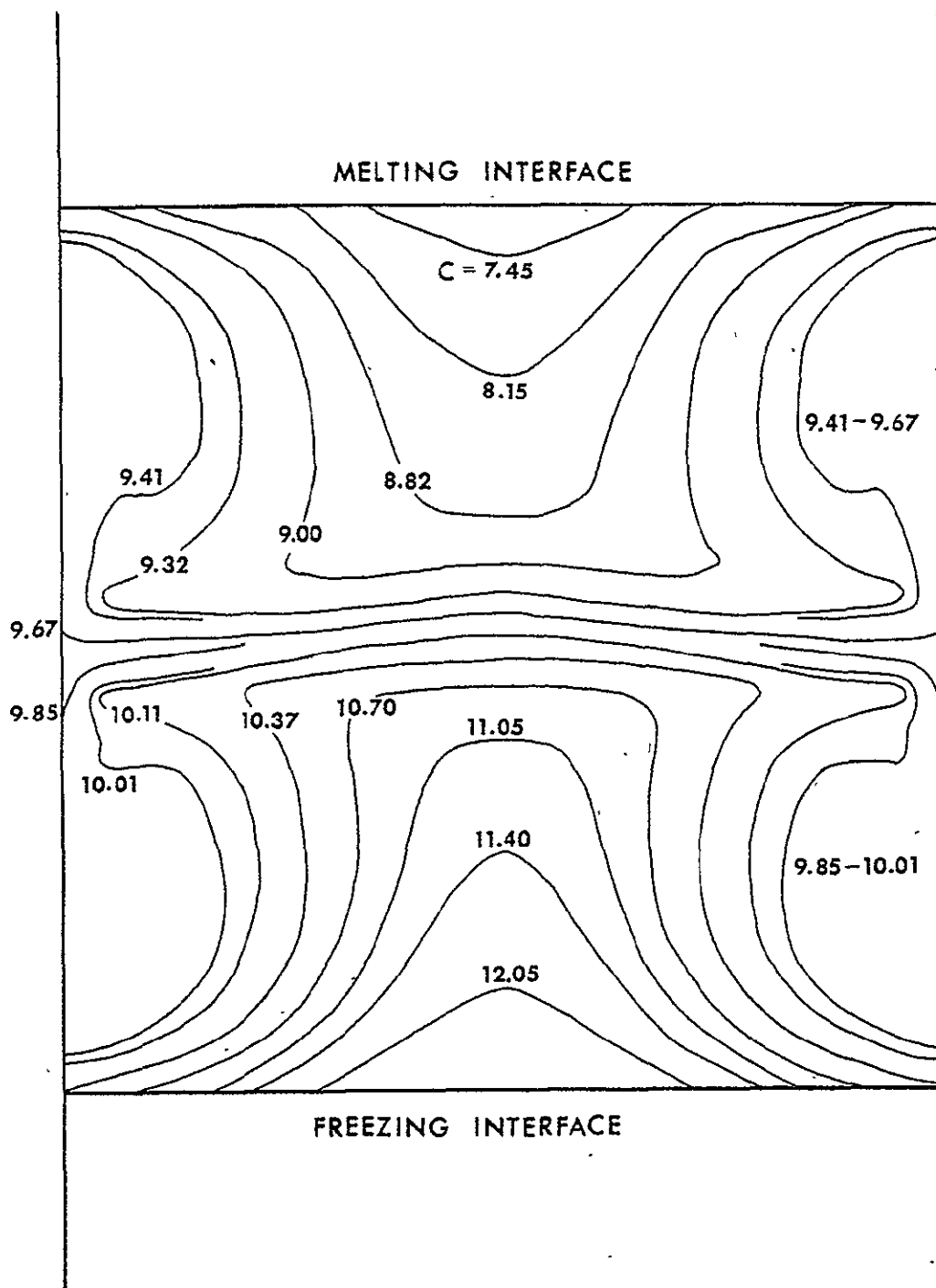


Figure 2. Dimensionless impurity concentration fields, $C = m/m_t$, in a silicon melt at steady state for a zone travel rate of $v_0 = 5 \text{ cm/hr.}$ with the same conditions and grid points as in Figure 1. $k_0 = 0.1$.

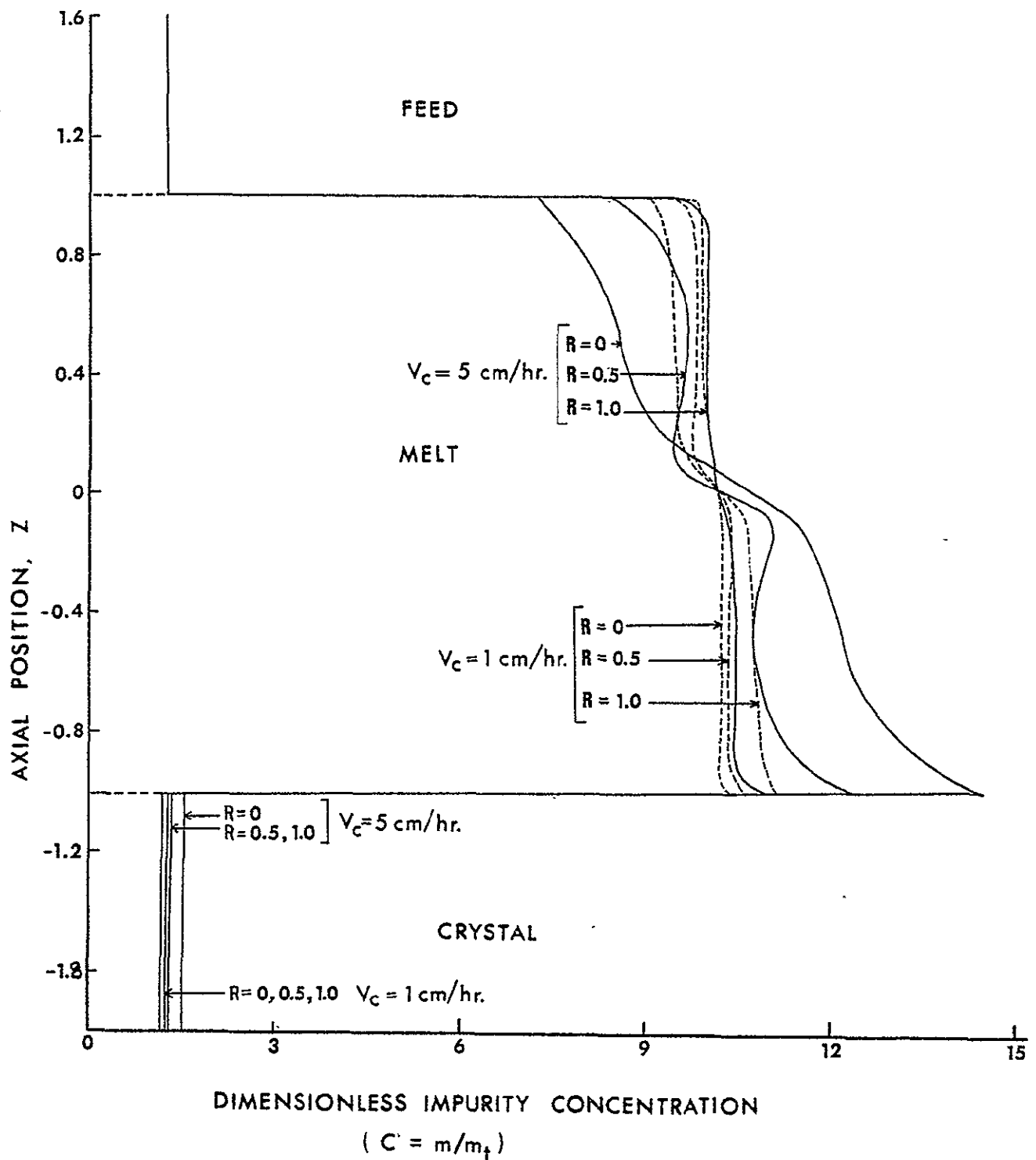


Figure 3. The calculated dimensionless impurity concentration profiles in the axial direction at $R = 0, 0.5$ and 1.0 under the same conditions and grid points as in Figure 1.

1c I. Summary of the surface tension driven convection in floating zone melting with various operating conditions.

M'^*	Gr_h	v_c (cm/hr)	Pr	Aspect Ratio (t/a)	Grid Points Used	Maximum Dimensionless Velocity Component of Fluid and its Location	Maximum Vorticity and its Location	Vortex Centers, Location and Direction of Rotation (+) for clockwise (-) for counterclockwise		Corresponding Figure (materials)
								1st	2nd	
Heating Method: Parabolic Temp. Profile (i.e., Radiant Heating)										
350	0	5	0.023	$\frac{1}{2}$ $a = 0.5$ cm	11 x 11	$V_z = 91$ $Z = 0.4$ $R = 1$	$\omega = 4545$ $Z = 0.5$ $R = 0.85$	(-) $Z = 0.35$ $R = 0.85$	—	Figure 4 (Silicon)
350	0	5	0.023	2 $a = 0.5$ cm	11 x 41	$V_z = 53$ $Z = 1.6$ $R = 1$	$\omega = 1517$ $Z = 2$ $R = 0.9$	(-) $Z = 1.5$ $R = 0.74$	—	Figure 8 (Silicon)
350	0	5	0.023	1 $l = 2$ cm	11 x 21	$V_z = 79$ $Z = 0.7$ $R = 1$	$\omega = 3295$ $Z = 1$ $R = 0.8$	(-) $Z = 0.70$ $R = 0.78$	—	Figure 22 (Silicon)
Heating Method: Ring Heat Source (i.e., Electron Beam Heating)										
350	0	5	0.023	$\frac{1}{2}$ $a = 0.5$ cm	11 x 11	$V_z = 98$ $Z = 0$ $R = 0.9$	$\omega = 3105$ $Z = 0.1$ $R = 0.9$	(-) $Z = 0.1$ $R = 0.9$	—	Figure 6 (Silicon)
350	0	5	0.023	2 $a = 0.5$ cm	11 x 41	$V_z = 56$ $Z = 0$ $R = 0.9$	—	(-) $Z = 0.1$ $R = 0.9$	(-) $Z = 0.9$ $R = 0.77$	Figure 10 (Silicon)
350	0	5	0.023	1 $a = 0.5$ cm	11 x 21	$V_z = 77$ $Z = 0$ $R = 0.9$	$\omega = 2402$ $Z = 0.1$ $R = 0.9$	(-) $Z = 0.1$ $R = 0.9$	(-) $Z = 0.48$ $R = 0.79$	Figure 7 in Annual Report [1] (Silicon)
350	0	5	0.023	1 $a = 0.5$ cm	21 x 41	$V_z = 69$ $Z = 0$ $R = 0.95$	$\omega = 3982$ $Z = 0.05$ $R = 0.95$	(-) $Z = 0.05$ $R = 0.95$	(-) $Z = 0.42$ $R = 0.80$	Figure 1 (Silicon)
350	0	5	0.023	1 $a = 2$ cm	11 x 21	$V_z = 83$ $Z = 0$ $R = 0.9$	$\omega = -2586$ $Z = 0.1$ $R = 0.9$	(-) $Z = 0.1$ $R = 0.9$	(-) $Z = 0.4$ $R = 0.8$	Figure 23 (Silicon)
22	0	5	0.34	1 $a = 0.5$ cm	11 x 21	$V_z = 7.3$ $Z = 0$ $R = 0.9$	$\omega = -205$ $Z = 0.1$ $R = 0.9$	(-) $Z = 0.1$ $R = 0.9$	—	Figure 27
35	0	5	12	1 $a = 0.5$ cm	11 x 21	$V_z = 11.9$ $Z = 0$ $R = 0.9$	$\omega = -377$ $Z = 0.1$ $R = 0.9$	(-) $Z = 0.1$ $R = 0.9$	—	Figure 30 (Sapphire)
140	0	5	12	1 $l = 0.5$ cm	11 x 21	$V_z = 52.7$ $Z = 0$ $R = 0.9$	$\omega = -1815$ $Z = 0.1$ $R = 0.9$	(-) $Z = 0.1$ $R = 0.9$	(-) $Z = 0.77$ $R = 0.84$	Figure 31 (Sapphire)

M*	Gr _h	v _c (cm/hr)	Pr	Aspect Ratio (L/a)	Grid Points Used	Maximum Dimensionless Velocity Component of Fluid and its Location	Maximum Vorticity and its Location	Vortex Centers, Location and Direction of Rotation (+) for clockwise (-) for counterclockwise		Corresponding Figure (materials)
								1st	2nd	
Heating Method: Ring Heat Source (i.e., Electron Beam Heating)										
350	3.1	5	0.023	1 a = 0.1 cm	11 × 21	V _r = 75.2 Z = 0 R = 0.9	ω = -2290 Z = 0.1 R = 0.9	(-) Z = 0.1 R = 0.9	(-) Z = 0.5 R = 0.78	Figure 15 (Silicon)
350	19.4	5	0.023	1 a = 0.25 cm	11 × 21	V _r = 75.8 Z = 0 R = 0.9	ω = -2314 Z = 0.1 R = 0.9	(-) Z = 0.1 R = 0.9	(-) Z = 0.52 R = 0.8	Figure 16 (Silicon)
350	310	5	0.023	1 a = 1 cm	11 × 21	V _r = 80 Z = 0 R = 0.9	ω = -2517 Z = 0.1 R = 0.9	(-) Z = 0.1 R = 0.9 (+) Z = -0.1 R = 0.9	(-) Z = 0.5 R = 0.78 (+) Z = -0.8 R = 0.8	Figure 17 (Silicon)
350	1240	5	0.023	1 a = 2 cm	11 × 21	V _r = 83.6 Z = 0 R = 0.9	ω = -2693 Z = 0.1 R = 0.9	(-) Z = 0.1 R = 0.9 (+) Z = -0.1 R = 0.9	(-) Z = 0.5 R = 0.78 (+) Z = -0.8 R = 0.9	Figure 18 (Silicon)
350	2790	5	0.023	1 a = 3 cm	11 × 21	V _r = 89 Z = 0 R = 0.9	ω = -2525 Z = 0.1 R = 0.9	(-) Z = 0.1 R = 0.9 (+) Z = -0.1 R = 0.9	(-) Z = 0.5 R = 0.78 (+) Z = -0.9 R = 0.9	Figure 19 (Silicon)
350	4960	5	0.023	1 a = 4 cm	11 × 21	V _r = 78.5 Z = 0.1 R = 1.0	ω = -2124 Z = 0.1 R = 0.9	(-) Z = 0.1 R = 0.9 (+) Z = -0.1 R = 0.9	(-) Z = 0.5 R = 0.78 (+) Z = -0.9 R = 0.9	Figure 20 (Silicon)
350	77.5	5	0.023	1 a = 2 cm	21 × 21	V _r = 88.7 Z = 0 R = 0.95	ω = -5247 Z = 0.05 R = 0.95	(-) Z = 0.05 R = 0.95	(-) Z = 0.5 R = 0.78	Figure 13 (Silicon)
350	1240	5	0.023	2 a = 2 cm	41 × 11	V _r = 59.2 Z = 0 R = 0.9	ω = -1815 Z = 0.1 R = 0.9	(-) Z = 0.1 R = 0.9 (+) Z = -0.1 R = 0.9	(-) Z = 0.5 R = 0.78 (+) Z = -1.3 R = 0.7	Figure 14 (Silicon)

$$M^* = \sigma \rho (T_o - T_m) a^3 / \mu^2 L^2$$

location of the vortex center near the heat source was found to be incorporated with the individual grid point nearest to the axial and the radial axis.

The dimensionless concentration field of the impurity, $C = m/m_t$, computed with 21×41 grid points is shown in Figure 2 and is essentially the same as that in Figure 18 in the Annual Report [1], except for an increased smoothness in the isoconcentration lines. The numerical values of concentration deviate slightly in the lower cell and deviate about 20 to 25% in the upper cell. The axial dimensionless concentration profiles at $R = 0, 0.5, 1.0$ are plotted in Figure 3. The wavy concentration profile at the melt free surface in previous Figure 19 [1] becomes smoother, as shown in Figure 3. This indicates that the wavy profile was associated with small errors at the individual grid points due to the coarse grid size. Another possible cause of numerical discrepancy may come from the coherent dependence of the interfacial gradients on the grid size, because the gradients are represented in a linear form in the finite difference equations.

C. Discussion

Grid refinement tests for the stream function, temperature and concentration fields for the case shown in previous Figures 7 and 18 [1] were carried out by doubling the grid points from 11×21 to 21×41 . The required computer time with 21×41 grid points was about 20 times more than that with 11×21 grid points. Not only did no additional vortex appear in the grid refinement tests, but also no fundamental difference in the overall patterns was found, although the concentration

profile and the vortex center near the heat source tended to be associated with the individual grid points with the coarser grid system. Convergence was much faster with the coarse mesh size than the finer mesh size.

We conclude that there is no significant advantage in using a finer mesh size at the expense of increased computer time, unless the flow pattern is very complex due to flow separation with many small vortices.

III. INFLUENCE OF THE ZONE LENGTH ON IMPURITY SEGREGATION

For an aspect ratio (ℓ/a) of other than one, the dimensionless surface tension parameter at the free melt surface, M' , should be defined in terms of the zone radius, a , and one half of the zone length, ℓ , such as

$$M' = \frac{\sigma \rho (T_o - T_m) a^3}{\mu \ell^2} \quad (1)$$

Computations were performed for a silicon zone of 1 cm diameter with the following variables:

- 1) $\ell/a = \frac{1}{2}$, $(T_o - T_m) = 0.0125^\circ\text{C}$, and $M' = 350$.
- 2) $\ell/a = 2$, $(T_o - T_m) = 0.2^\circ\text{C}$, and $M' = 350$.

The heating modes employed in the present calculations are:

- 1) Parabolic surface temperature profile, which is assumed to be a radiant heating mode.
- 2) Ring heat source at the center of the zone with electron beam heating.

The results for the computed streamline, temperature and concentration fields are shown in Figures 4 through 11. The vortex cells are stretched in the long zone ($l/a = 2$) and contracted in the short zone ($l/a = \frac{1}{2}$) and no additional multiple cells are generated. However, in a short zone with electron beam heating, the secondary vortex cell, which appears in the long zone, is combined with the primary vortex cell to make a single cell near the ring heat source, as shown in Figure 6.

The impurity incorporation into the crystal is plotted in Figure 12. It shows that the radial distribution of the impurity in the grown crystal is not sensitive to the mode of heating, but is sensitive to the zone length. The radial inhomogeneity of impurity is greater for the crystal with the shorter zone, which is expected from the fact that the convection of the melt near the center of zone is relatively weak compared with that in a long zone. The isotherms near the melt/solid interfaces are curved in the short zone, while those in the long zone are nearly flat. This, in turn, reflects the tendency for the interfaces to deviate from a flat to a curved shape as the zone length is decreased. The characteristics of the flow patterns and the physical and operational parameters are summarized in Table I.

IV. COMBINED SURFACE TENSION DRIVEN AND BUOYANCY DRIVEN CONVECTION

As discussed earlier, M' is the primary factor characterizing the surface tension driven flow regardless of the size of the zone when the buoyancy effect is neglected. However, the buoyancy effect is expected to increase as the diameter of the zone increases, since the

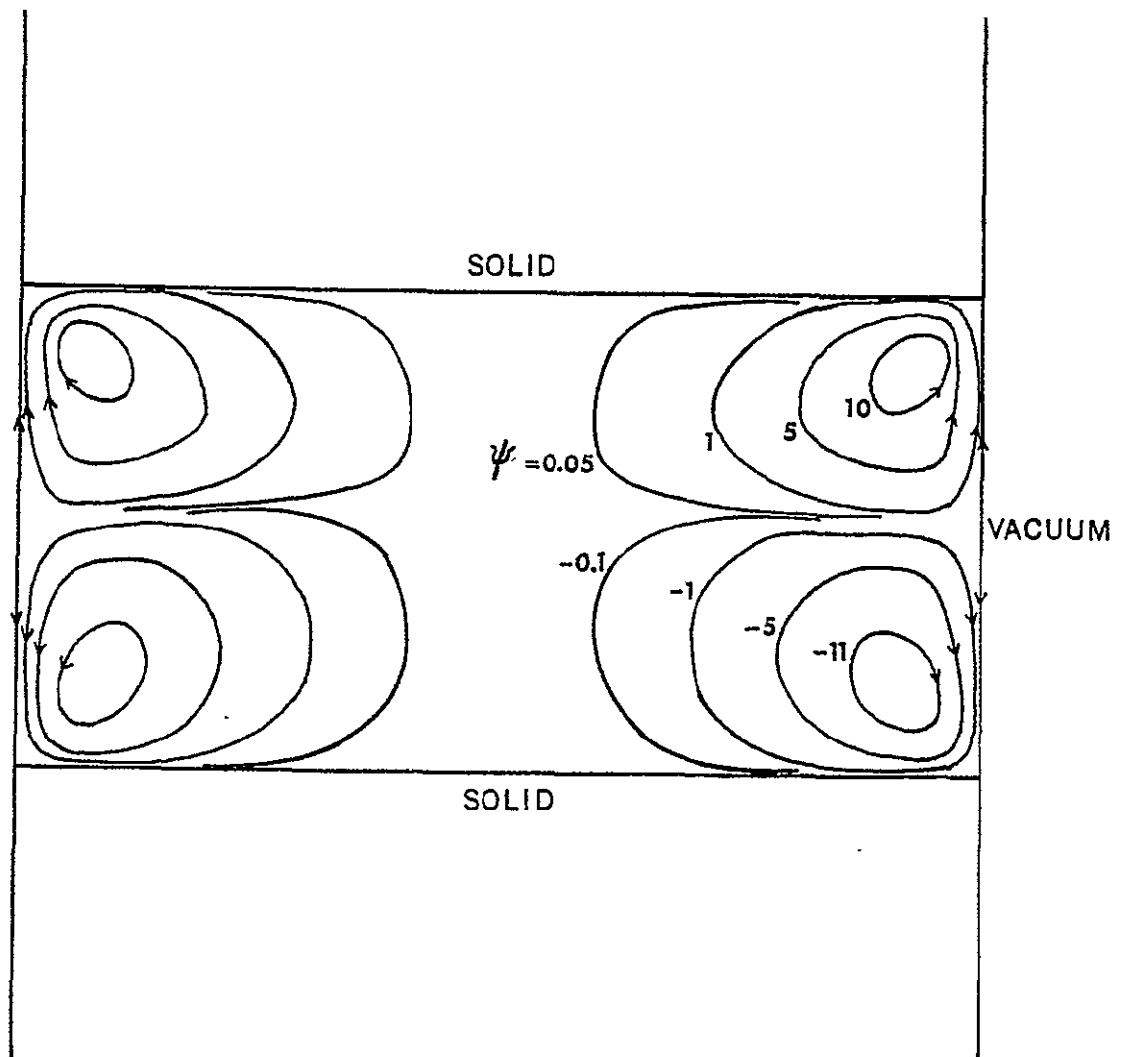


Figure 4. Computed dimensionless streamlines, ψ for surface tension driven flow in a floating zone at zero gravity with a parabolic temperature profile on the free melt surface with $(T_0 - T_m) = 0.0125^\circ\text{C}$, $a = 0.5$ cm, $l = 0.25$ cm, $M' = 350$, and $v_0 = 5$ cm/hr. Calculations performed with 11×11 grid.

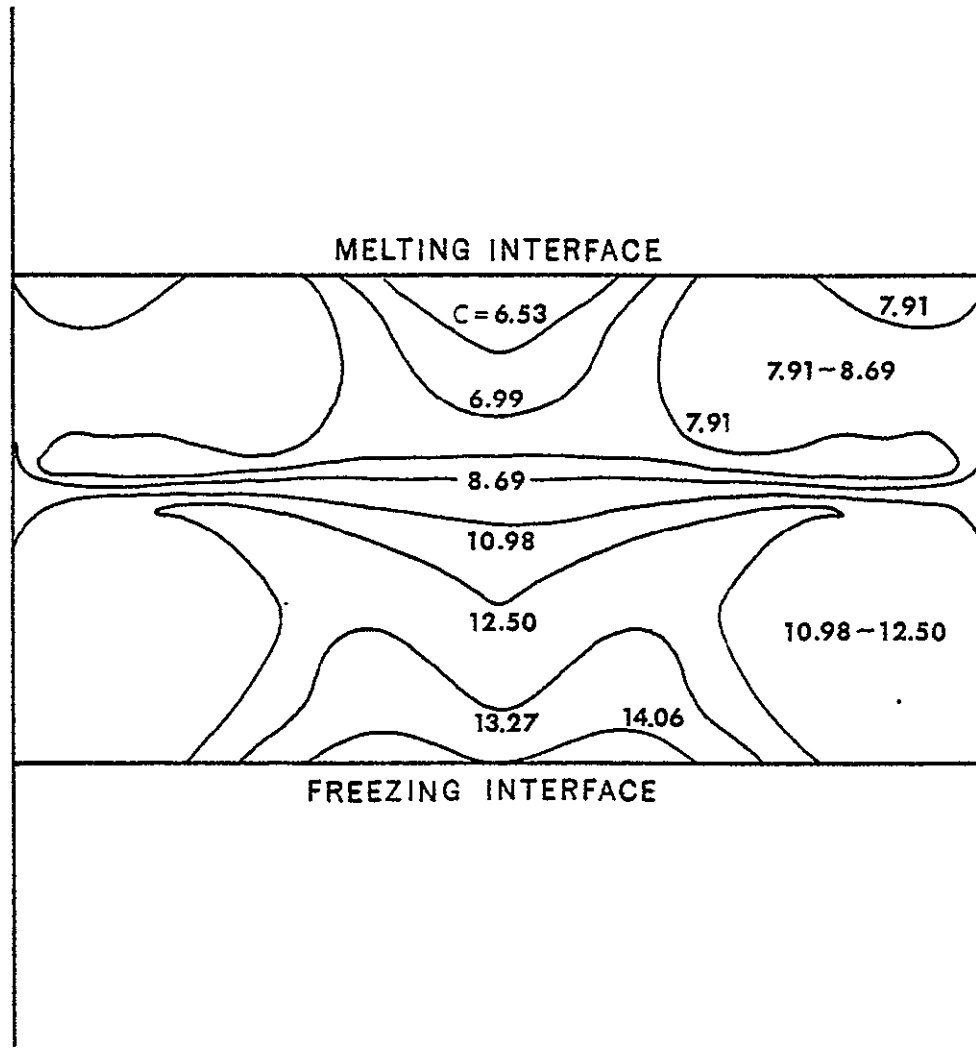


Figure 5. Computed dimensionless impurity concentration fields, $C = m/m_t$ at steady state in a silicon melt for the same conditions as in Figure 4 with $Sc = 5.0$, $k_0 = 0.1$, and $D = 7.6 \times 10^{-4} \text{ cm}^2/\text{sec}$.

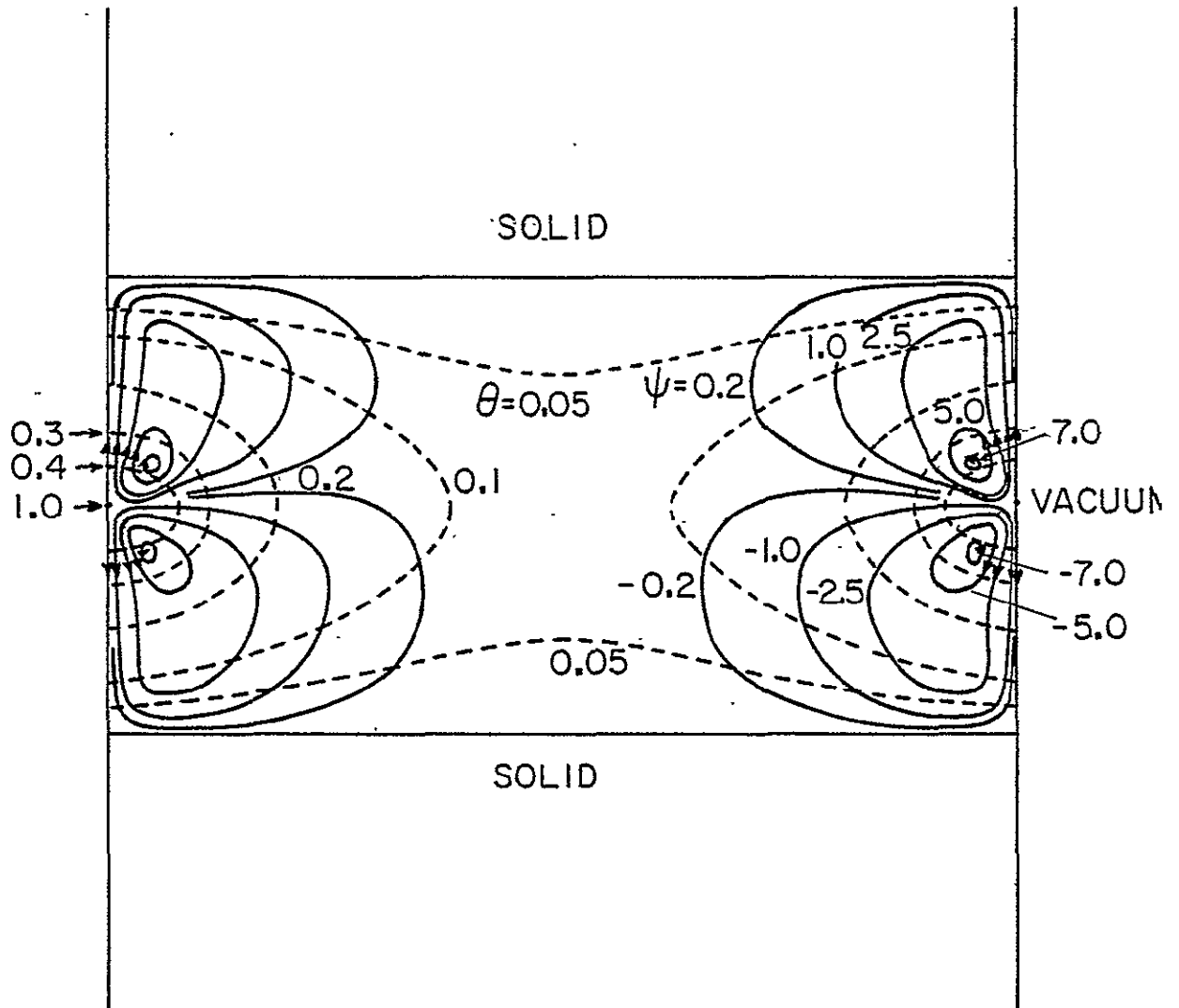


Figure 6. Computer calculated isotherms, θ (dotted lines) and streamlines, ψ (solid lines) for surface driven flow in floating zone melting at zero gravity, using the computed temperature fields for electron beam heating of silicon with $(T_o - T_m) = 0.0125^\circ\text{C}$, $T_c = T_m$, $\delta_s = 0.3$, $a = 0.5$ cm, $l = 0.25$ cm, $M' = 350$, $Pr = 0.023$, $v_o = 5$ cm/hr, and $\theta = (T - T_m)/(T_o - T_m)$. Calculations performed with 11×11 grid.

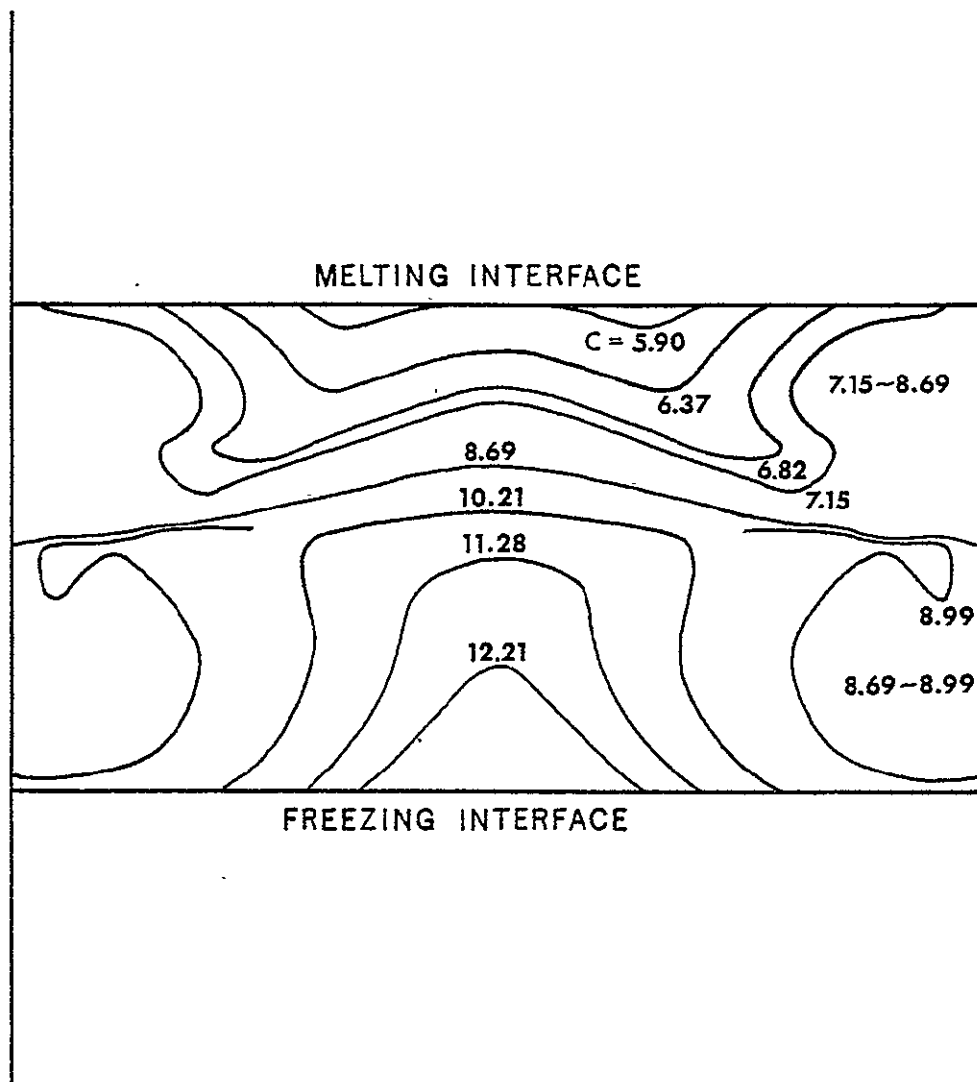


Figure 7. Computed dimensionless impurity concentration fields, $C = m/m_t$ at steady state in a silicon melt for the same conditions as in Figure 6 with $Sc = 5.0$, $k_0 = 0.1$, and $D = 7.6 \times 10^{-4} \text{ cm}^2/\text{sec}$.

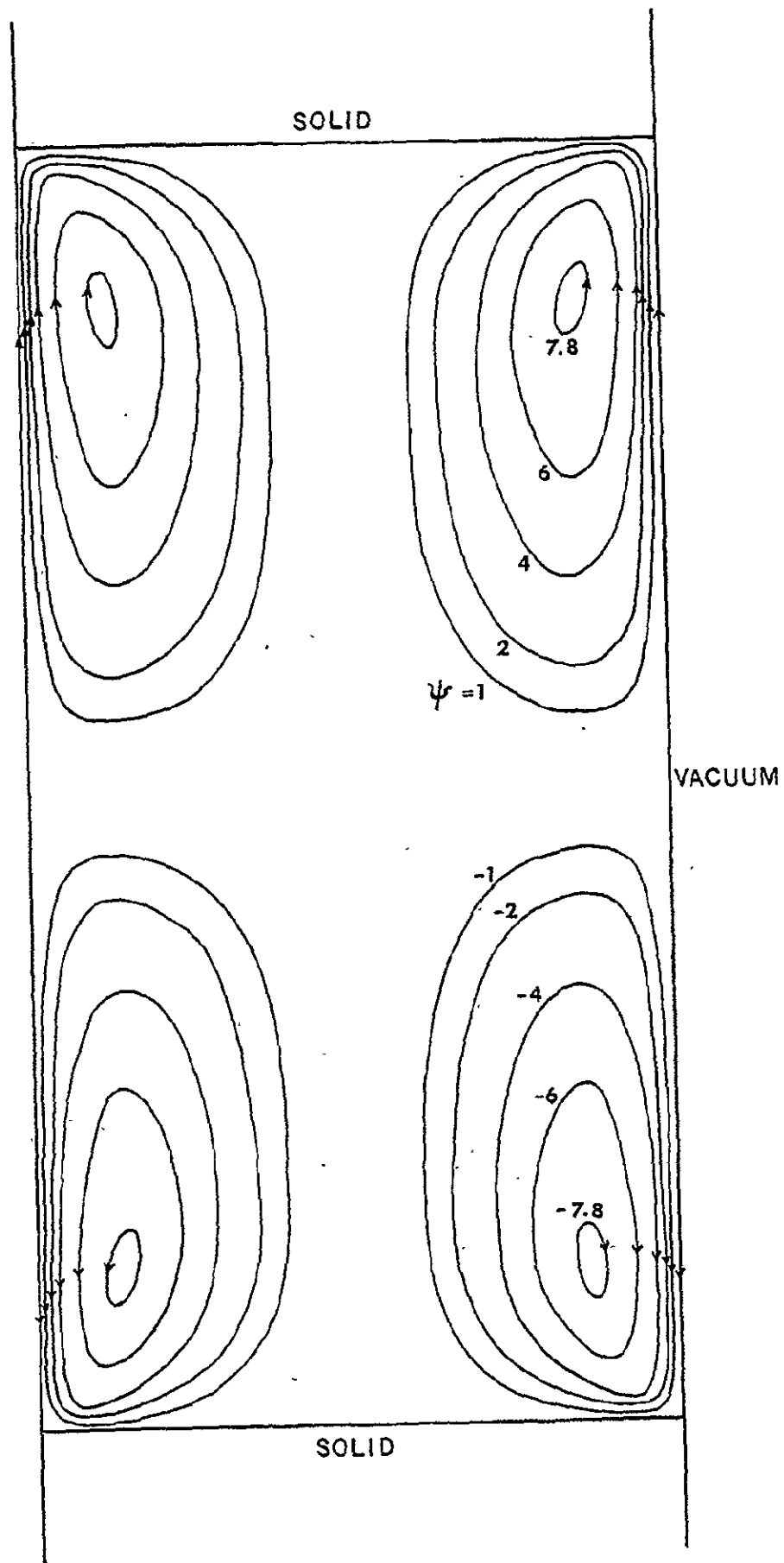


Figure 8. Computed dimensionless streamlines, ψ , for surface tension driven flow in a floating zone at zero gravity with a parabolic temperature profile on the free melt surface with $(T_o - T_a) = 0.2^\circ\text{C}$, $a = 0.5$ cm, $\ell = 1$ cm, $M' = 350$, and $v_o = 5$ cm/hr. Calculations performed with 11×41

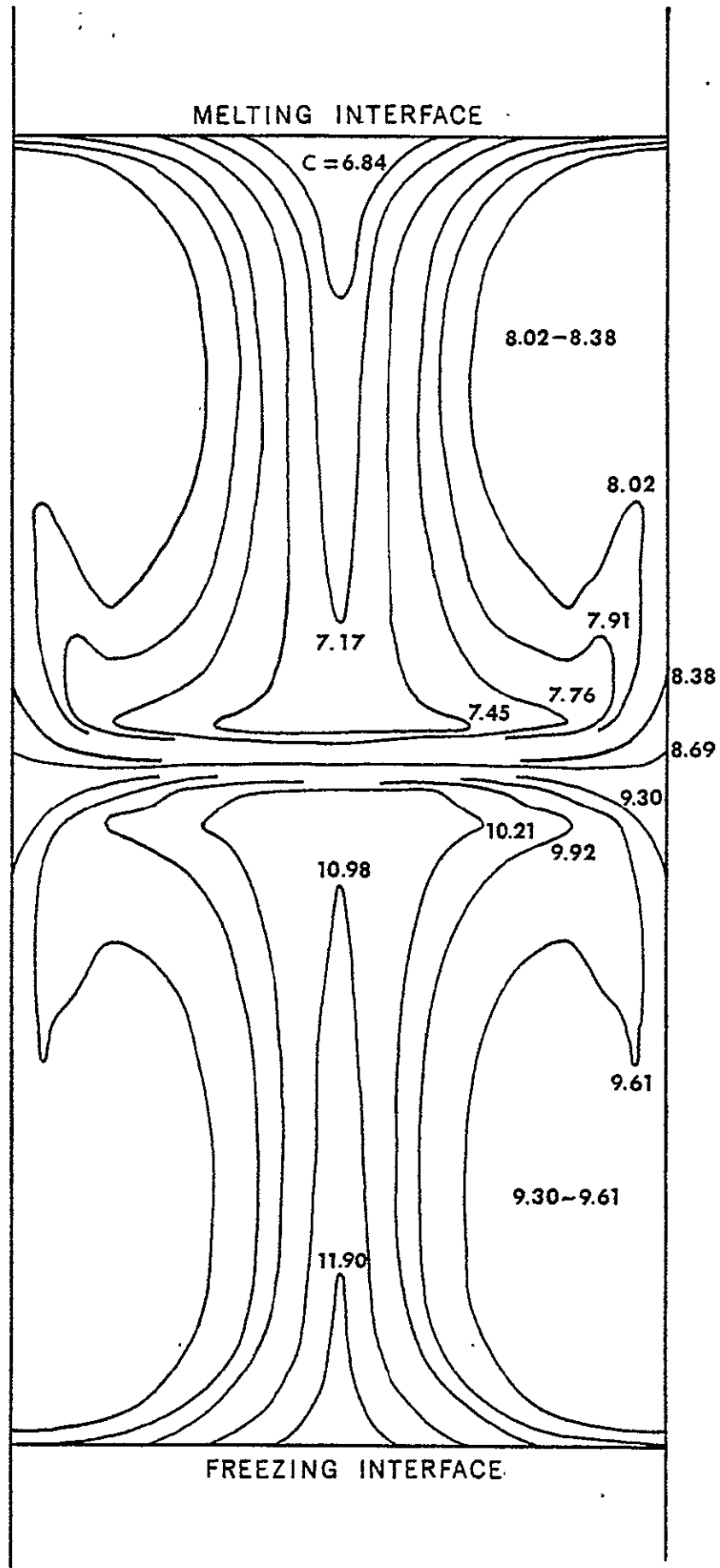


Figure 9. Computed dimensionless impurity concentration fields, $C = m/m_i$, at steady state in a silicon melt for the same conditions as in Figure 8, with $Sc = 5.0$, $k_0 = 0.1$, and $D = 7.6 \times 10^{-4} \text{ cm}^2/\text{sec}$.

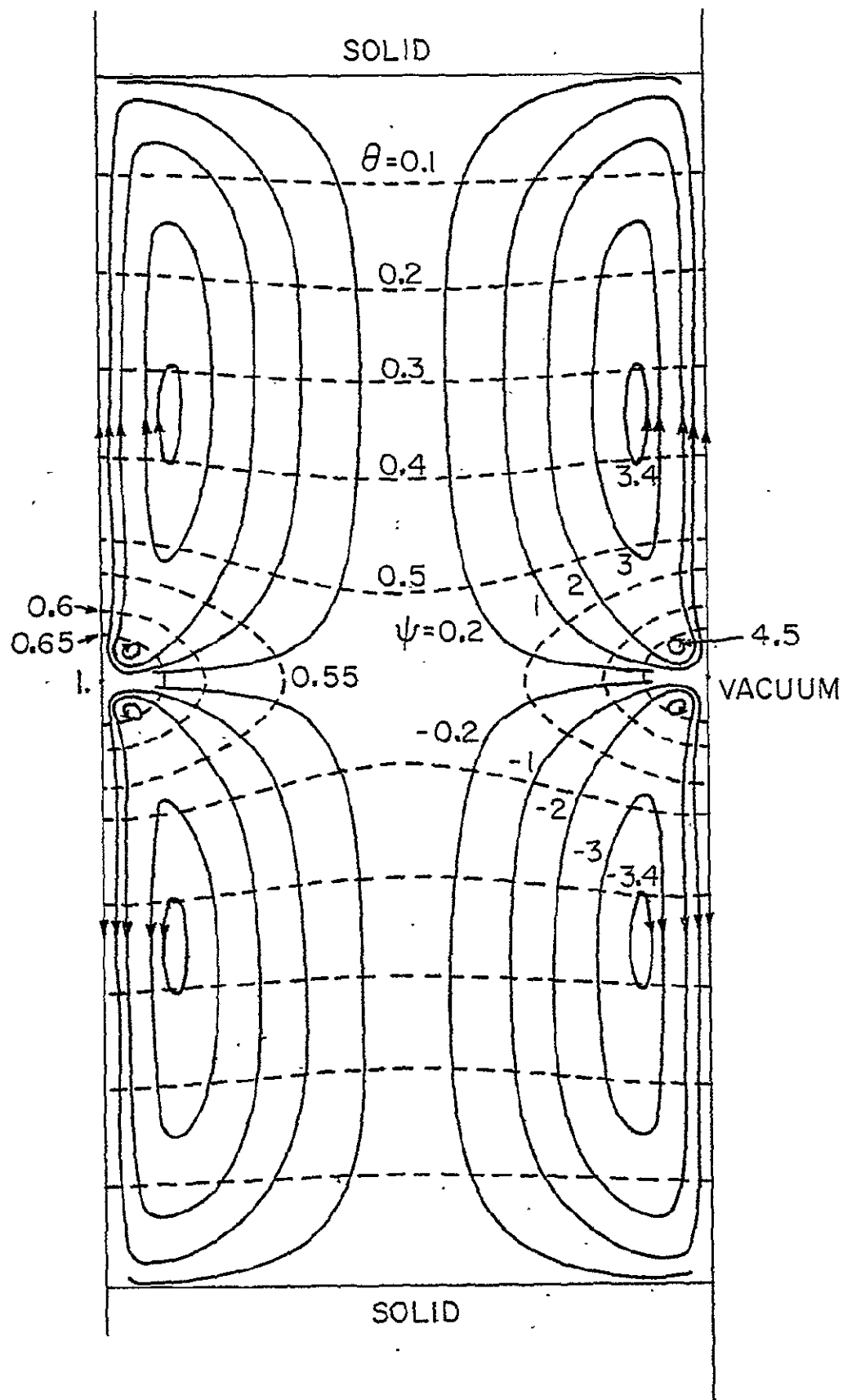


Figure 10. Computer calculated isotherms, θ (dotted lines), and streamlines, ψ (solid lines) for surface tension driven flow in floating zone melting at zero gravity, using the computed temperature fields for electron beam heating of silicon with $(T_o - T_m) = 0.2^\circ \text{C}$, $T_o = T_m$, $\delta_o = 0.3$, $a = 0.5 \text{ cm}$, $\ell = 1 \text{ cm}$, $M' = 350$, $Pr = 0.023$, $v_o = 5 \text{ cm/hr}$, and $\theta = (T - T_m)/(T_o - T_m)$. Calculations performed with 11×41 grid.

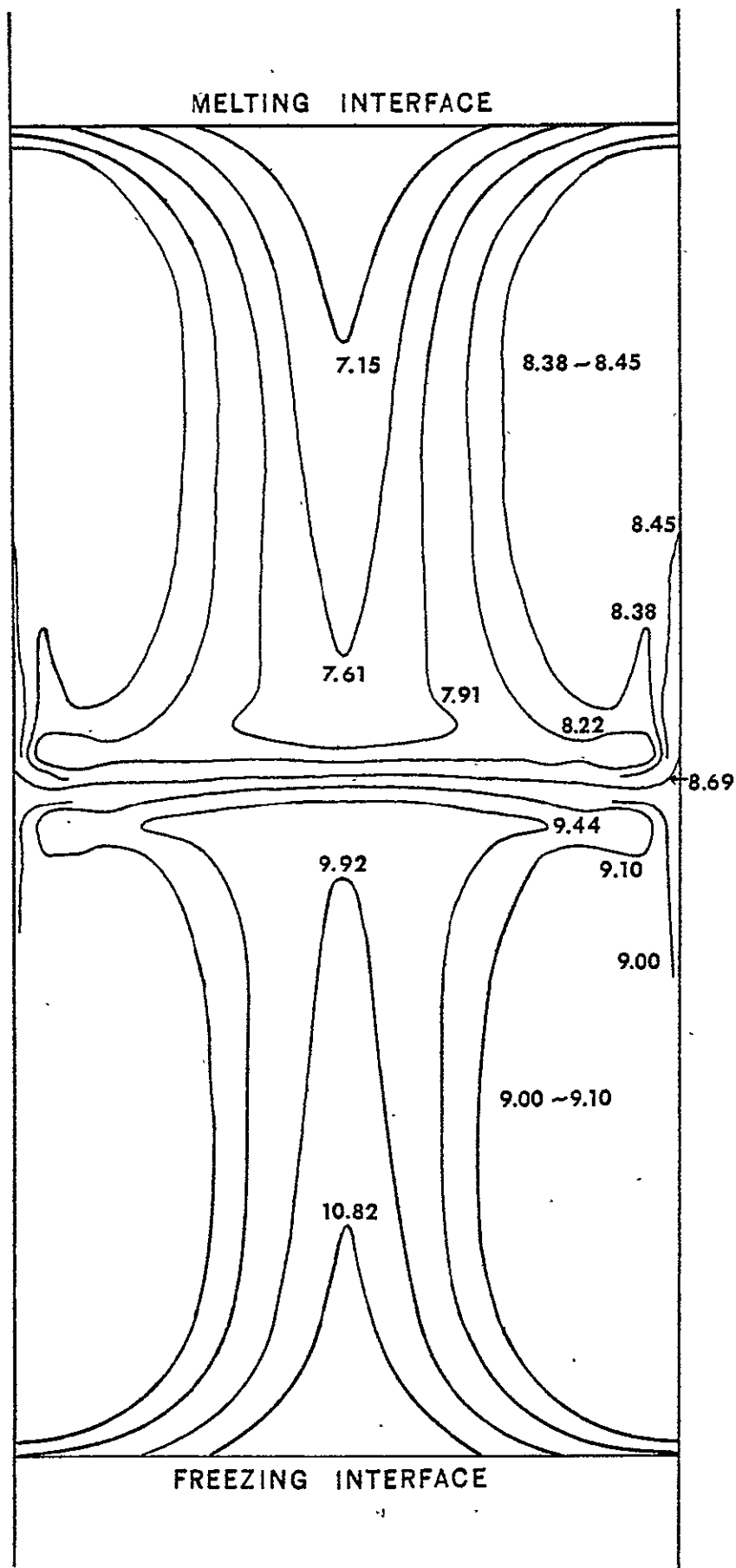


Figure 11. Computed dimensionless impurity concentration fields, $C = m/m_t$, at steady state in a silicon melt for the same conditions as in Figure 10 with $Sc = 5.0$, $k_o = 0.1$, and $D = 7.6 \times 10^{-4} \text{ cm}^2/\text{sec}$.

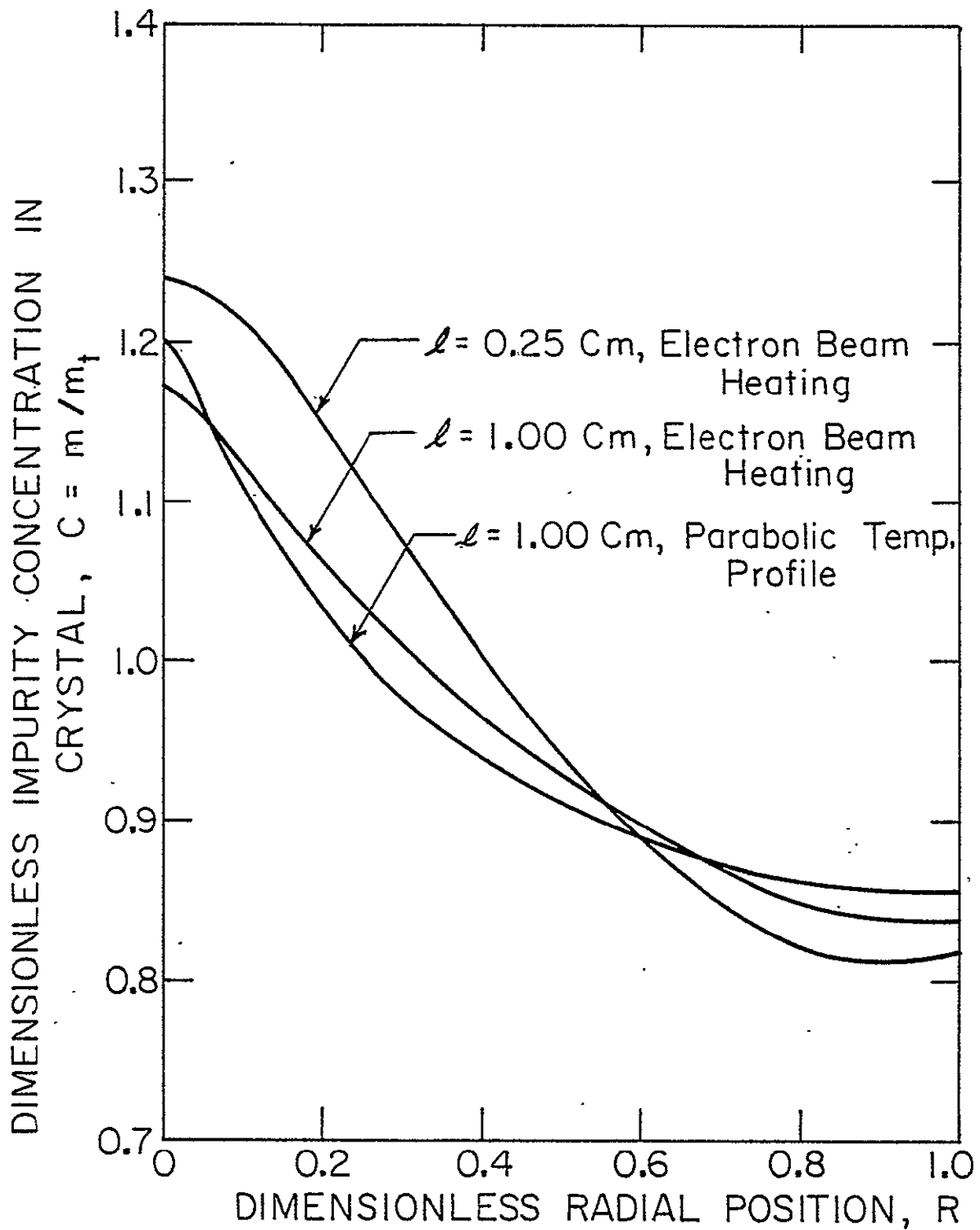


Figure 12. Radial impurity concentration profiles in the crystal at steady state freezing rate of 5 cm/hr. calculated from the interfacial concentration in Figures 7, 9, and 11 for interfacial distribution coefficient of $k_0 = 0.1$.

buoyancy driven flow is due to the volume effect while the surface tension driven flow is due to the free liquid surface area effect.]

In order to define a new parameter for combined surface tension driven and buoyancy driven flow, the dimensionless velocities of flow were redefined based on the reference velocity. The parameters derived from the momentum equation are Gr_h/M'^2 and $1/M'$. The combined surface tension driven and buoyancy driven flows are compared with pure surface tension driven flow as a function of Gr_h/M'^2 and the geometry of zone.

A. Model for Analysis of the Combined Convection

In the present study, we derived parameters combining Gr_h and M' in order to obtain a better correlation for the combined surface tension driven and buoyancy driven flow. Employing the reference velocity defined as $v_o = \sigma(T_o - T_m)a^2/\mu\ell^2$, the surface tension parameter M' is absorbed in the momentum equation instead of in the free melt boundary condition. By defining $\tau = tv_o/a$, $V_r = v_r/v_o$, $V_z = v_z/v_o$, $Z = z/a$, and $R = r/a$, the following momentum equation is obtained through the similar operations made in the annual Progress Report:

$$\frac{\partial w}{\partial \tau} + \frac{\partial(V_r w)}{\partial R} + \frac{\partial(V_z w)}{\partial Z} = \frac{Gr_h}{M'^2} \frac{\partial \theta}{\partial R} + \frac{1}{M'} \left\{ \frac{\partial^2 w}{\partial Z^2} + \frac{\partial}{\partial R} \left(\frac{1}{R} \frac{\partial(Rw)}{\partial R} \right) \right\} \quad (2)$$

where

$$V_r = \frac{1}{R} \frac{\partial \psi}{\partial Z}, \quad V_z = -\frac{1}{R} \frac{\partial \psi}{\partial R}, \quad M' = \frac{\rho \sigma (T_o - T_m) a^3}{\mu^2 \ell^2},$$

and

$$Gr_h = \frac{g \beta (T_o - T_m) a^3}{\nu^2} \quad \text{and} \quad w = \frac{1}{R} \left(\frac{\partial^2 \psi}{\partial R^2} - \frac{1}{R} \frac{\partial \psi}{\partial R} + \frac{\partial^2 \psi}{\partial Z^2} \right).$$

The parameter, Gr_h/M'^2 , can be separated into the property parameter and the operation parameter as follows:

$$\frac{Gr_h}{M'^2} = \underbrace{\left\{ \frac{g\beta\mu^2\rho^2}{\sigma^2} \right\}}_{\text{property parameter}} \underbrace{\left\{ \frac{l^4}{(T_o - T_m)a^3} \right\}}_{\text{operating parameter}} \quad (3)$$

B. Influence of the Zone Length

Inspecting Equation (3) the buoyancy effect is expected to increase as the zone length, l , increases. Calculations were performed for both short and long zones of silicon using the following values:

<u>Zone Diameter</u> <u>in cm</u>	<u>Zone Length</u> <u>in cm</u>	$(T_o - T_m)$ <u>in °C</u>	<u>M</u>	<u>Gr_h</u>
2	1	0.00625	350	77.5
2	4	0.1	350	1240.

The calculated streamlines and isotherms are shown in Figures 13 and 14. For the identical value of $M' = 350$, the buoyancy effect was pronounced in a long zone and negligible in a short zone.

C. Influence of the Zone Diameter

When the zone aspect ratio is one (i.e., $a = l$), Gr_h/M'^2 becomes proportional to $a/(T_o - T_m)$. This suggests that the buoyancy effect increases as the zone diameter increases and/or the temperature difference in the zone decreases. Therefore, the relative influence of the buoyancy driven convection is expected to increase as the efficiency of thermal insulation of the zone increases.

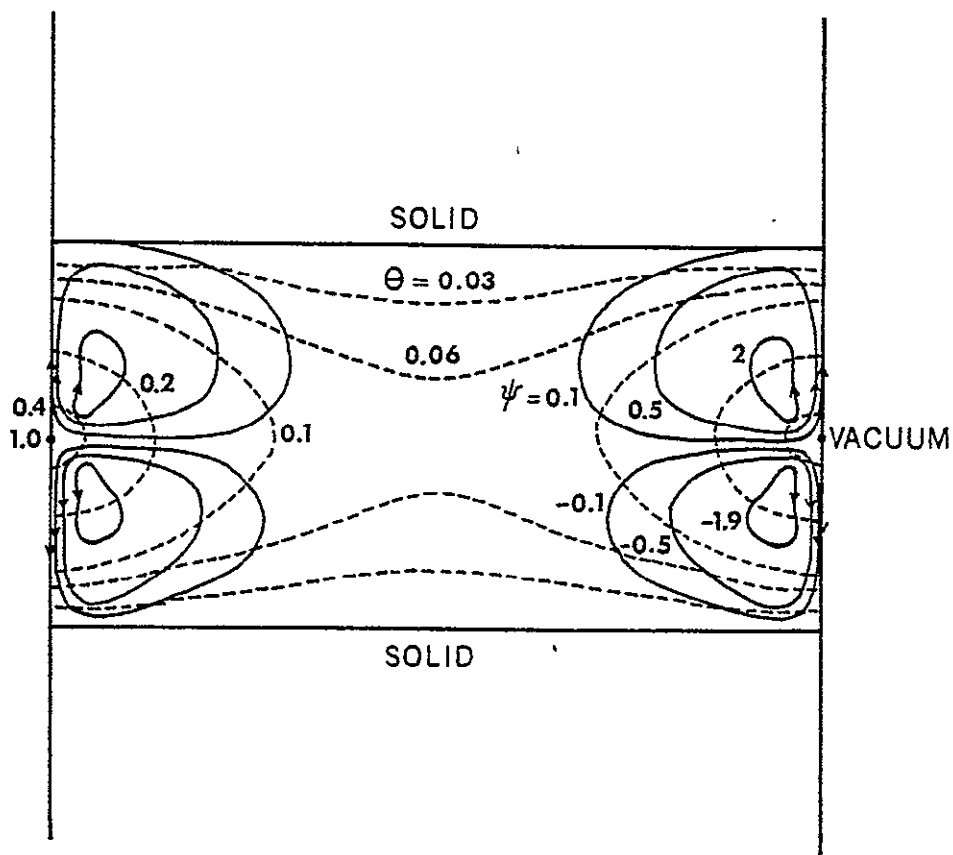


Figure 13. Computer calculated isotherms, θ (dotted lines) and streamlines, ψ (solid lines) for surface tension driven flow in floating zone melting at the gravity of earth, using the computed temperature fields for electron beam heating of silicon with $(T_o - T_m) = 0.00625^\circ\text{C}$, $T_o = T_m$, $\delta_s = 0.3$, $a = 1$ cm, $l = 0.5$ cm, $M' = 350$, $Pr = 0.023$, $Gr_h = 77.5$, $v_c = 5$ cm/hr., and $\theta = (T - T_m)/(T_o - T_m)$. Calculation performed with 21×21 grid.

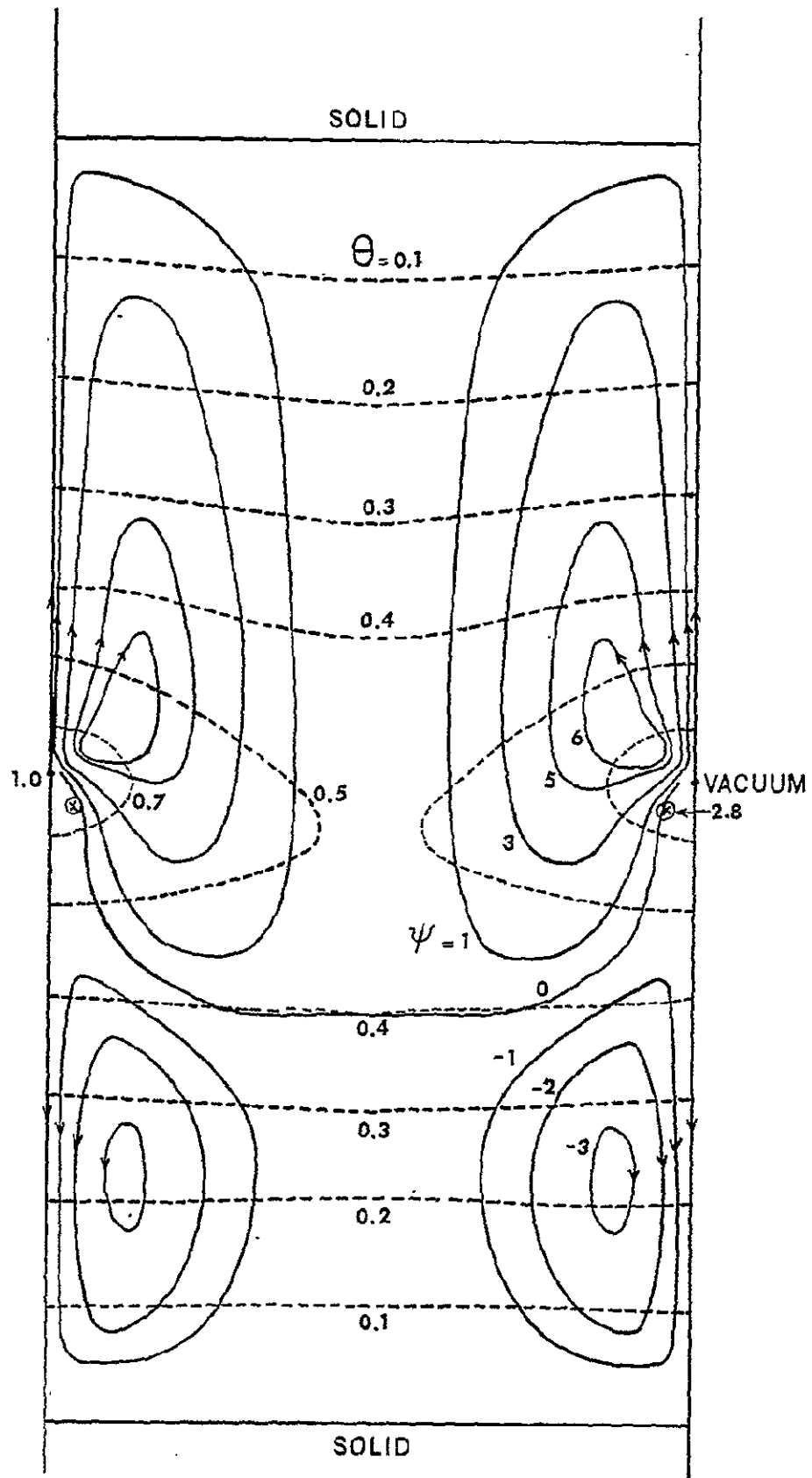


Figure 14. Same conditions as in Figure 22 except $(T_o - T_a) = 0.1^\circ\text{C}$, $a = 1\text{ cm}$, $l = 2\text{ cm}$, and $Gr_h = 1240$. Calculations performed with a 41×11 grid.

Both the combined convection and the pure surface tension driven convection were calculated with various zone diameters and M' , and were compared in terms of the ratio of Nusselt numbers, Γ at the center of the freezing interface. That is

$$\Gamma = \frac{\text{Nusselt No. at } 1g}{\text{Nusselt No. at } 0g} = \frac{Nu_g}{Nu_0} . \quad (4)$$

The values used in the calculations for electron beam heated floating zone melting of silicon with the aspect ratio of one ($a=1$) are shown in Table II.

For silicon zones of 0.2 cm to 8 cm diameter with $M' = 350$, earth's gravity and various ring heat source temperatures depending on the size of the zone, the convection patterns for combined buoyancy driven and surface tension driven flow as a function of zone diameter are shown in Figures 15 through 20. As the zone diameter increases, the vortex cell below the center of the zone gradually diminishes while the convection of the vortex cell above is significantly enhanced. In order to relate the buoyancy effect to the zone diameter, the Nusselt number (i.e., dimensionless temperature gradient) as the solid/melt interface is calculated with and without the buoyancy effect. At the center of the interface, the Nusselt number was most sensitive to the buoyancy effect and least sensitive at the periphery of the interface. The values of Γ with $M'=350$ are plotted as a function of the zone diameter in Figure 21. Note that the buoyancy effect becomes negligible when the diameters of the zone are below about 0.8 cm.

Table II. Ratio of Nusselt numbers at 1g and 0g for various experimental conditions

Zone Diameter in cm	$(T_o - T_m)$ in °C	M'	Gr_h	ψ_{max} at 0g	$Nu_g / Nu_0 = \Gamma$
2	.0125	175	155	4.11	.3705/.3689 = 1.004
4	.00625	175	2480	3.37	.7454/.6623 = 1.125
10	.0025	175	3875	4.89	1.220/.8945 = 1.364
0.2	.25	350	3.1	6.64	.3881/.3880 = 1.00
0.5	.10	350	19.4	6.68	.3848/.3842 = 1.002
1	.05	350	77.5	6.84	.3815/.3765 = 1.013
2	.025	350	310	7.19	.3775/.3521 = 1.072
4	.0125	350	1240	7.47	.4304/.3626 = 1.187
6	.00833	350	2790	7.86	.5985/.4551 = 1.315
8	.00625	350	4960	7.84	.7735/.5626 = 1.375
0.2	.5	700	6.2	10.76	.3614/.3604 = 1.003
0.5	.2	700	38.8	10.22	.3648/.3539 = 1.031
1	.1	700	155	10.10	.4198/.3402 = 1.234
2	.05	700	620	9.67	.5123/.3282 = 1.561
4	.025	700	2480	11.31	.5058/.2982 = 1.696
6	.0166	700	5580	11.08	.5534/.3094 = 1.789
0.5	.30	1050	58.1	11.64	.3052/.2966 = 1.029
1	.15	1050	232.5	11.54	.3974/.2936 = 1.354

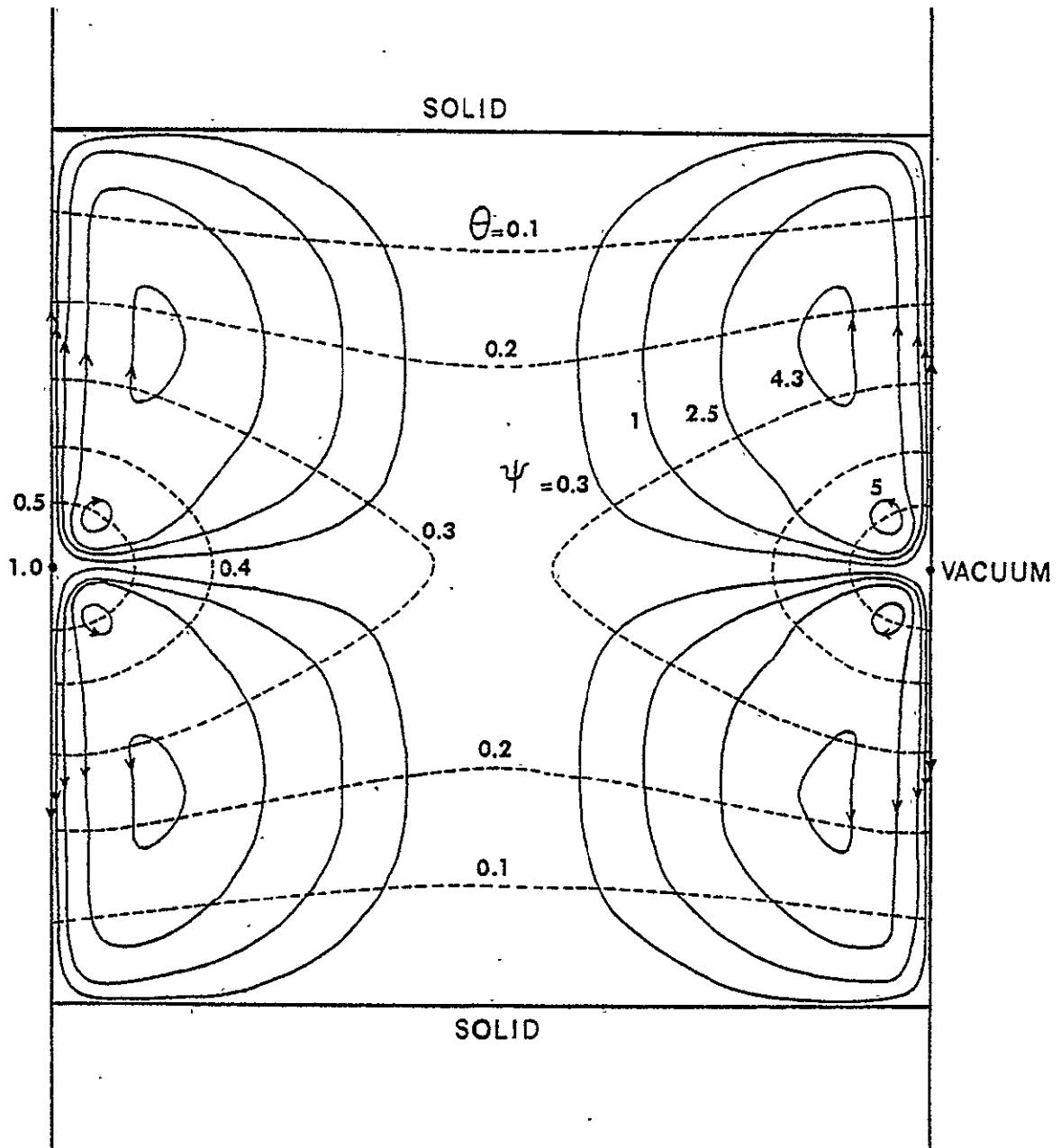


Figure 15. Computer calculated isotherms, θ (dotted lines) and streamlines, ψ (solid lines) for surface tension driven flow in floating zone melting at the gravity of earth, using the computed temperature fields for electron beam heating of silicon with $(T_o - T_m) = 0.25^\circ\text{C}$, $T_c = T_m$, $g_s = 0.3$, $a = b = 0.1$ cm, $M' = 350$, $Pr = 0.023$, $Gr_h = 3.1$, $v_c = 5$ cm/hr, and $\theta = (T - T_m) / (T_o - T_m)$.

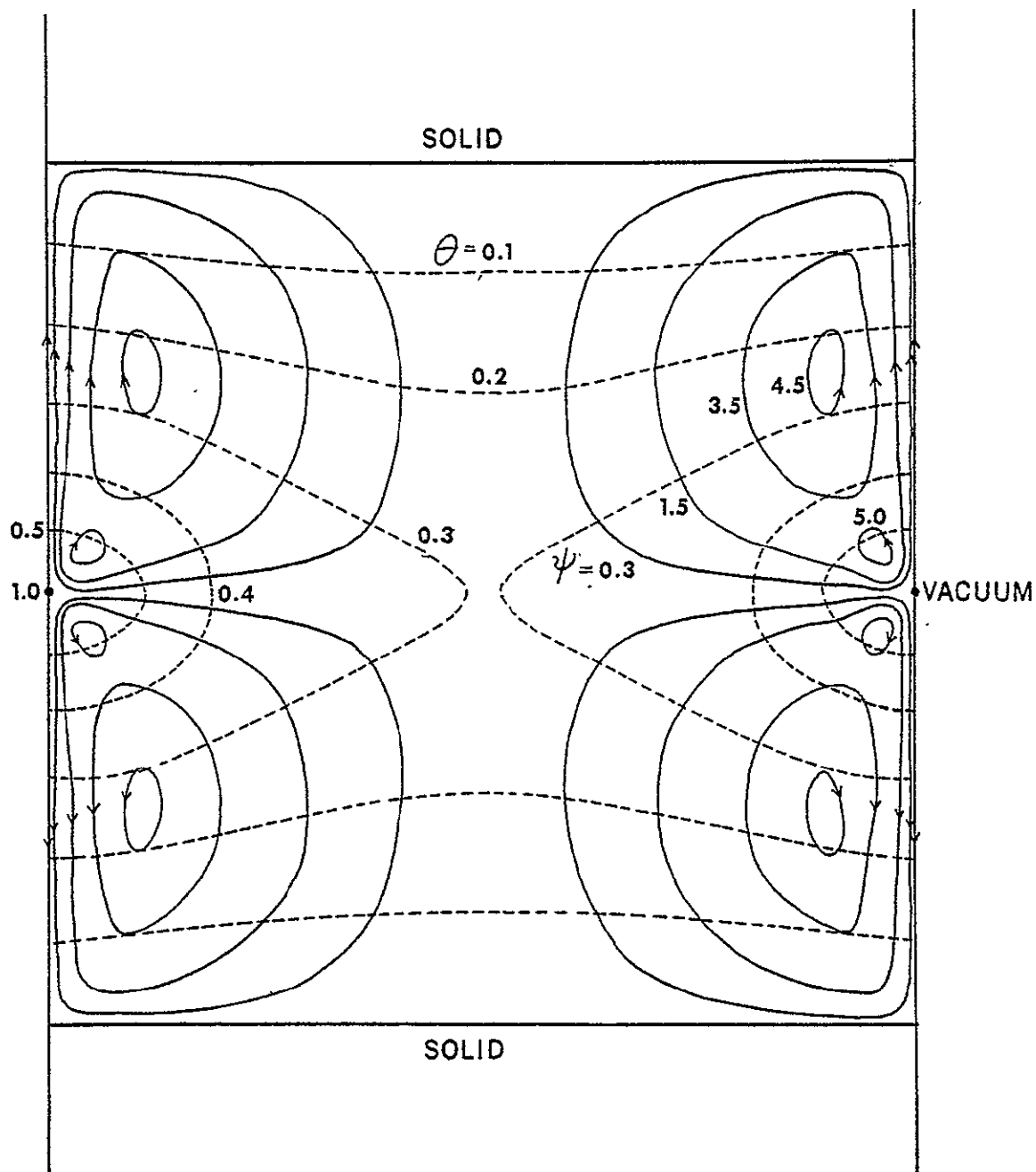


Figure 16. Same conditions as in Figure 15 except $(T_o - T_a) = 0.1^\circ\text{C}$, $a = \ell = 0.25$ cm, and $Gr_h = 19.4$.

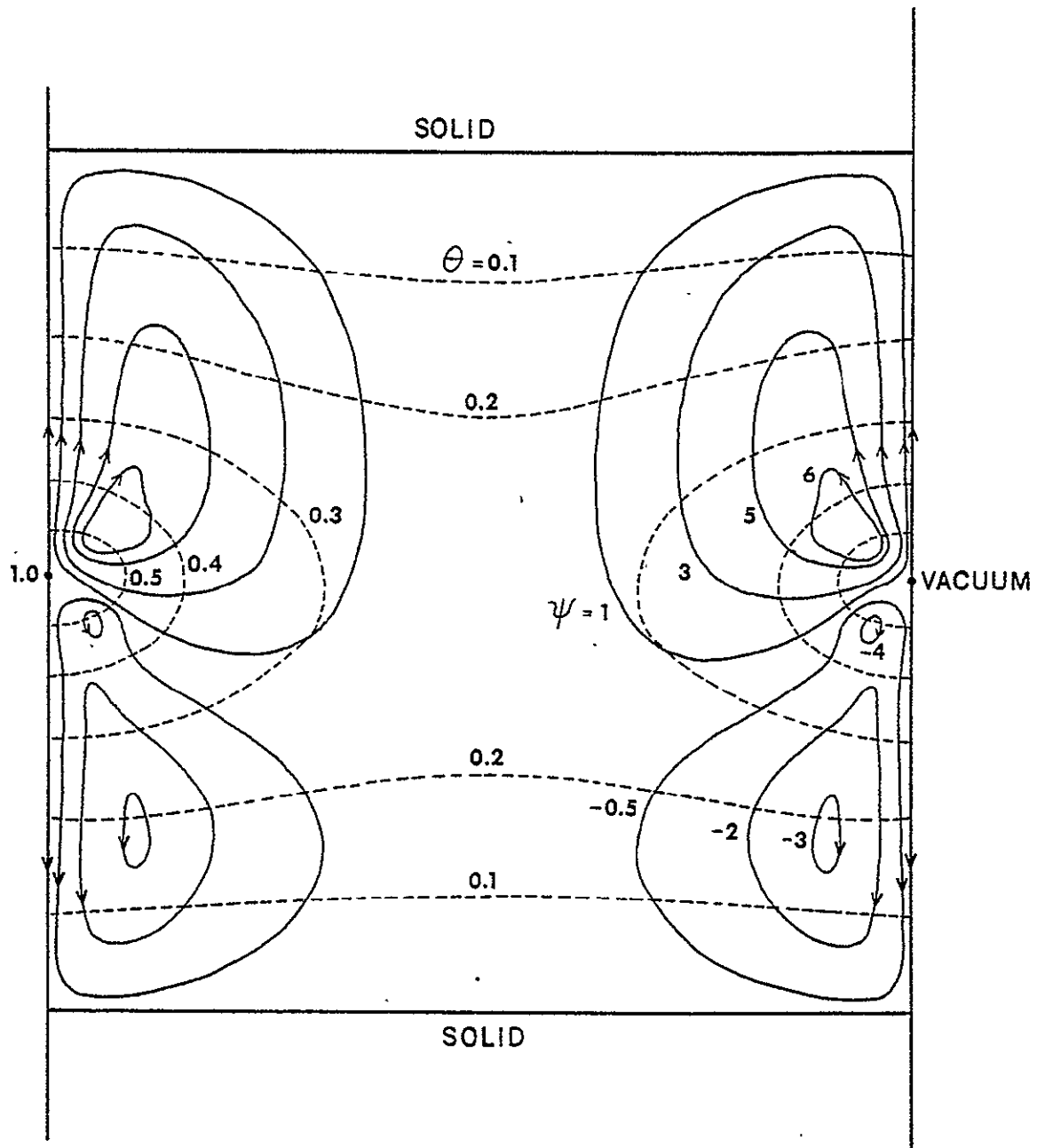


Figure 17. Same conditions as in Figure 15 except $(T_o - T_a) = 0.1^\circ\text{C}$, $a = l = 1\text{ cm}$ and $Gr_h = 310$.

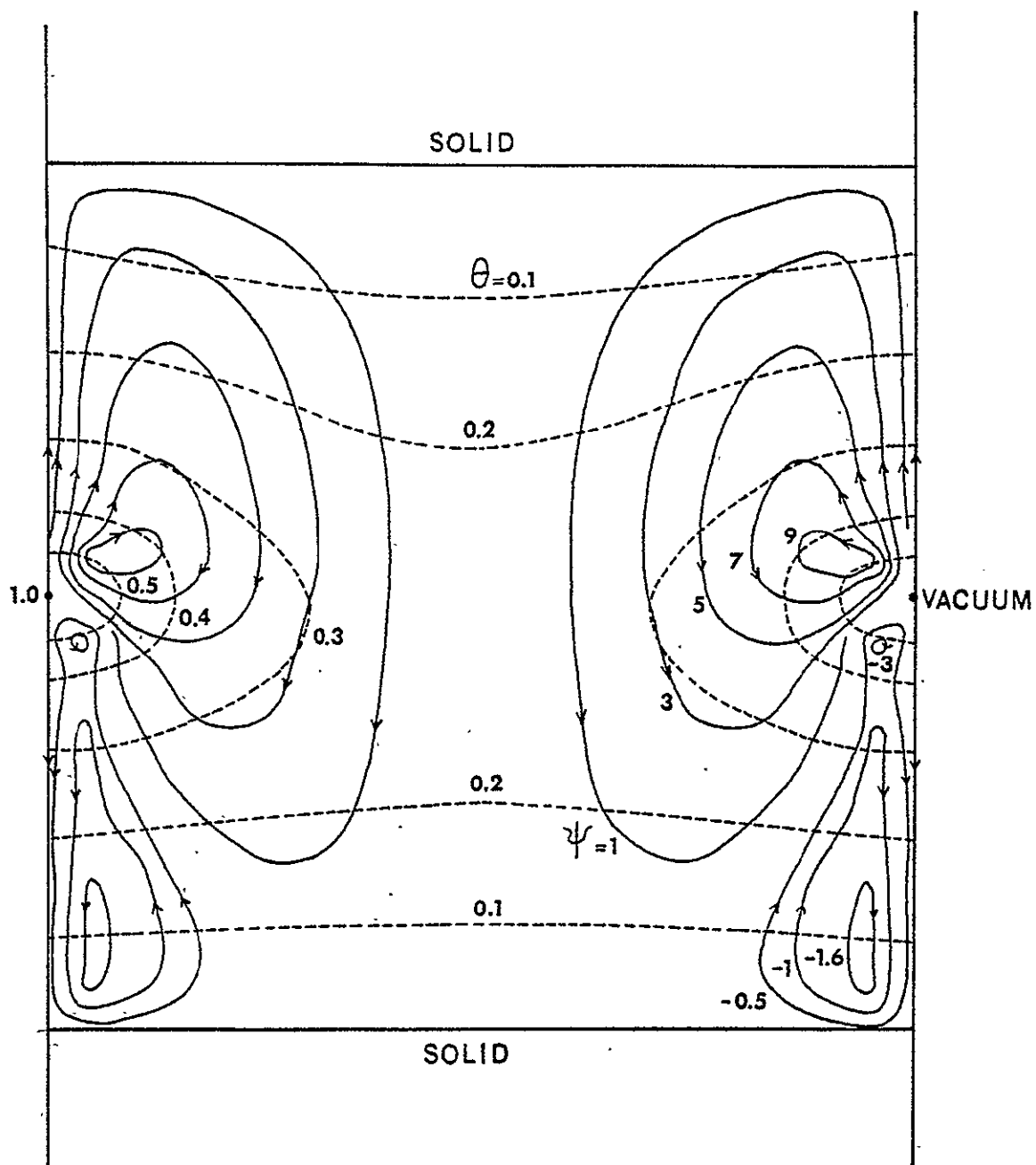


Figure 18. Same conditions as in Figure 15 except $(T_o - T_m) = 0.0125^\circ\text{C}$, $a = b = 2\text{ cm}$ and $Gr_h = 1240$.

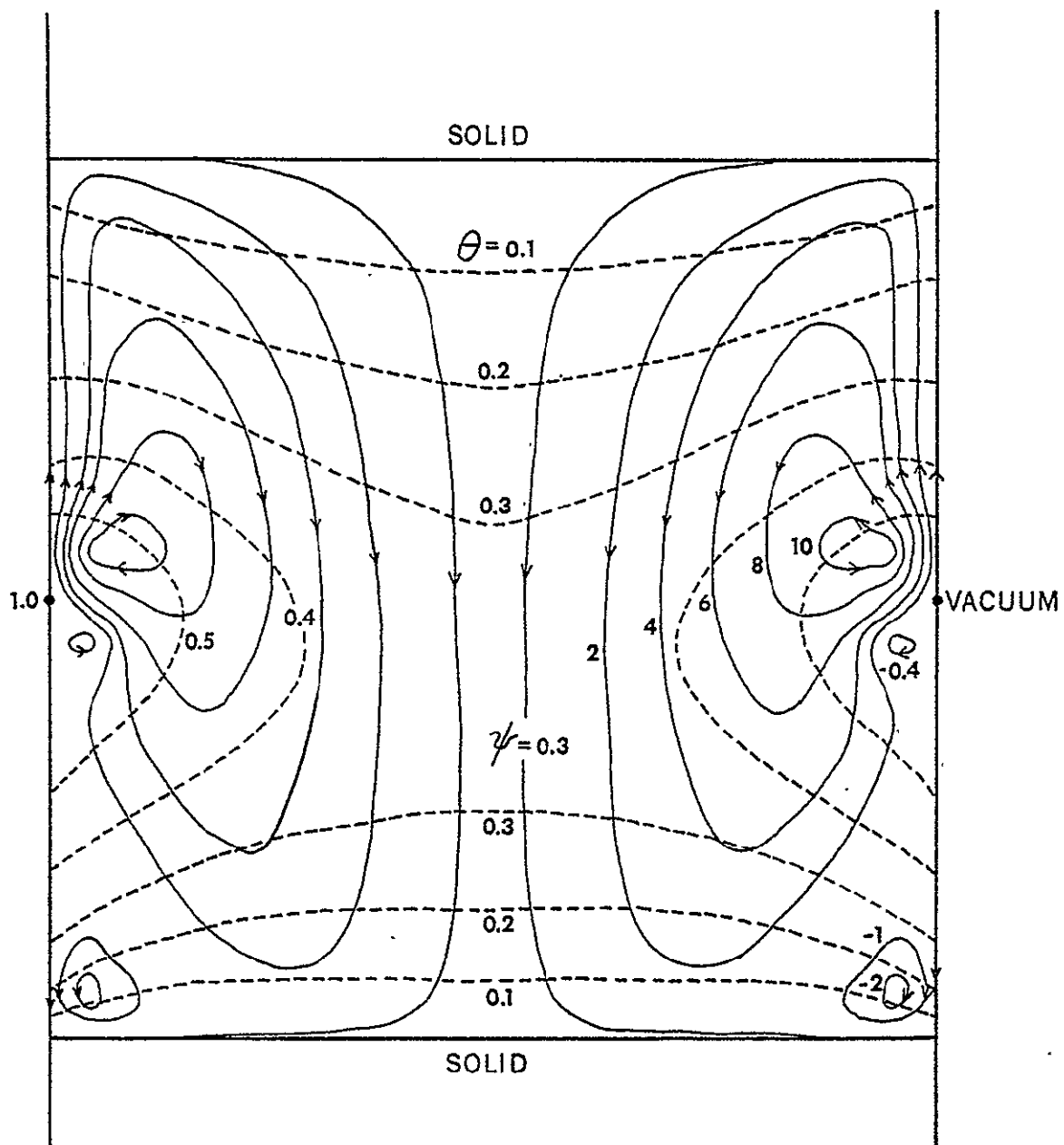


Figure 20. Same conditions as in Figure 15 except $(T_o - T_a) = 0.00625^\circ\text{C}$, $a = b = 4\text{ cm}$ and $Gr_h = 4960$.

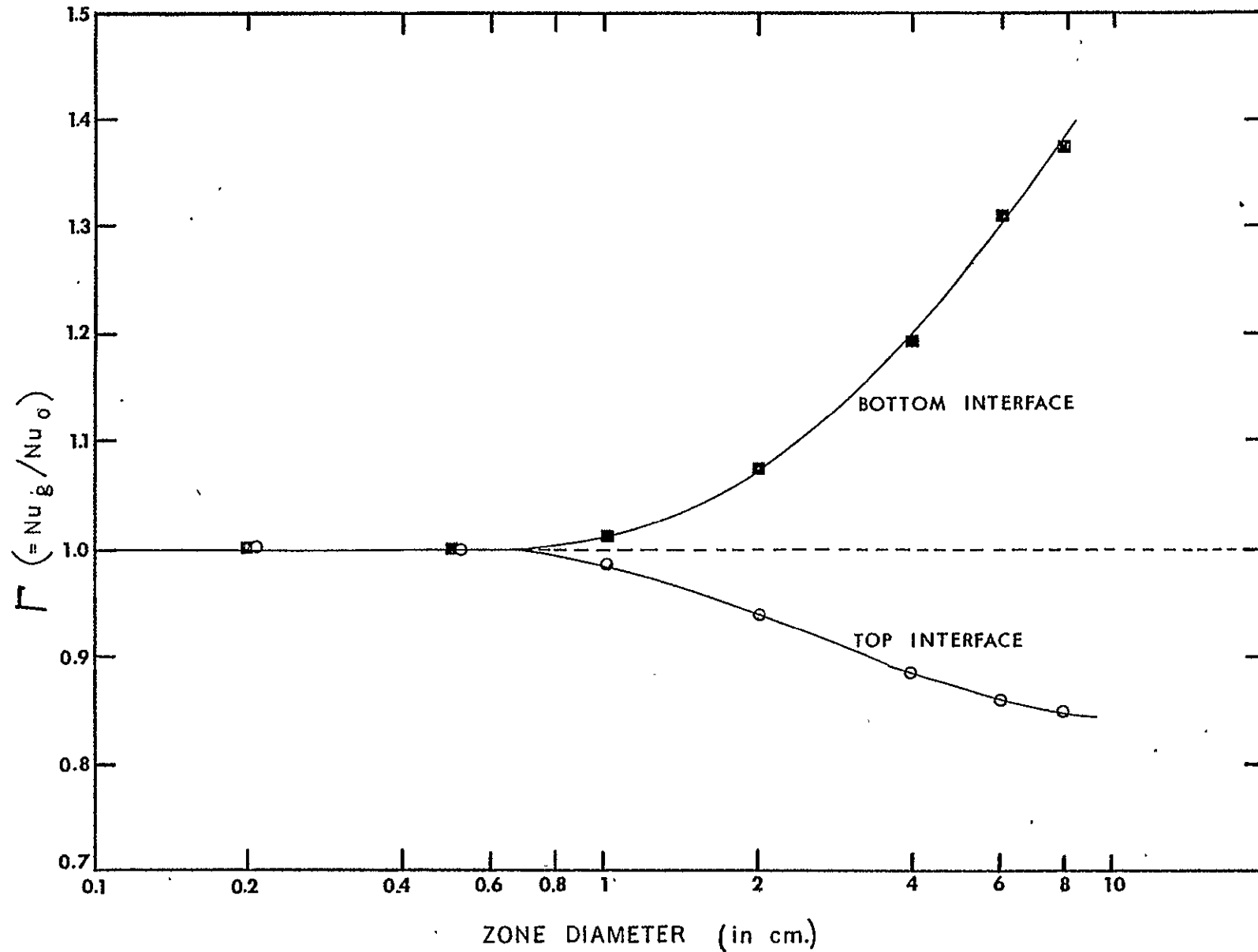


Figure 21. The ratio of the Nusselt number of combined surface tension driven and buoyancy driven flow at 1 g to that of pure surface tension driven flow at the center of the interfaces versus the zone diameter for the floating zone melting of silicon with electron beam heating, $T_c = T_m$, $\delta_i = 0.3$, $M' = 350$, $Pr = 0.023$, and $v_e = 5$ cm/hr.

Figures 22 and 23 illustrate the effect of increased zone diameter on the pure surface tension driven flow at zero g for a silicon zone of 4 cm diameter with $\ell = 2$ cm, $(T_o - T_m) = 0.0125^\circ\text{C}$ and $M' = 350$. Both a parabolic surface temperature profile and a ring heat source at the center of zone were employed. The computed streamlines with parabolic temperature profile are shown in Figure 22. The simultaneous solution for streamlines and temperature fields with electron beam heater are shown in Figure 23. The convection patterns shown in Figures 22 and 23 are similar to those obtained with a smaller zone diameter, shown in Figures 3 and 7 of the First Annual Progress Report [1]. The similarity in convection patterns indicates that M' is the primary factor characterizing the surface tension driven flow regardless of the size of the zone for a given material. It should be noted, however, that as the diameter of the zone increases, M' will actually increase in proportion to about the square of the increase in the zone diameter, since the temperature difference $(T_o - T_m)$ will also increase in proportion to the increase in zone diameter. Therefore, the increase in zone diameter from 1 to 4 cm has the same effect of increasing M' from 350 to about 1400, and convection would become stronger in the larger zone.

The maximum stream functions for pure surface tension driven flow, ψ_{\max} , are plotted as a function of M' in Figure 24. The relationship is correlated by the following expression:

$$\psi_{\max} = 0.199 (M')^{0.6} . \quad (5)$$

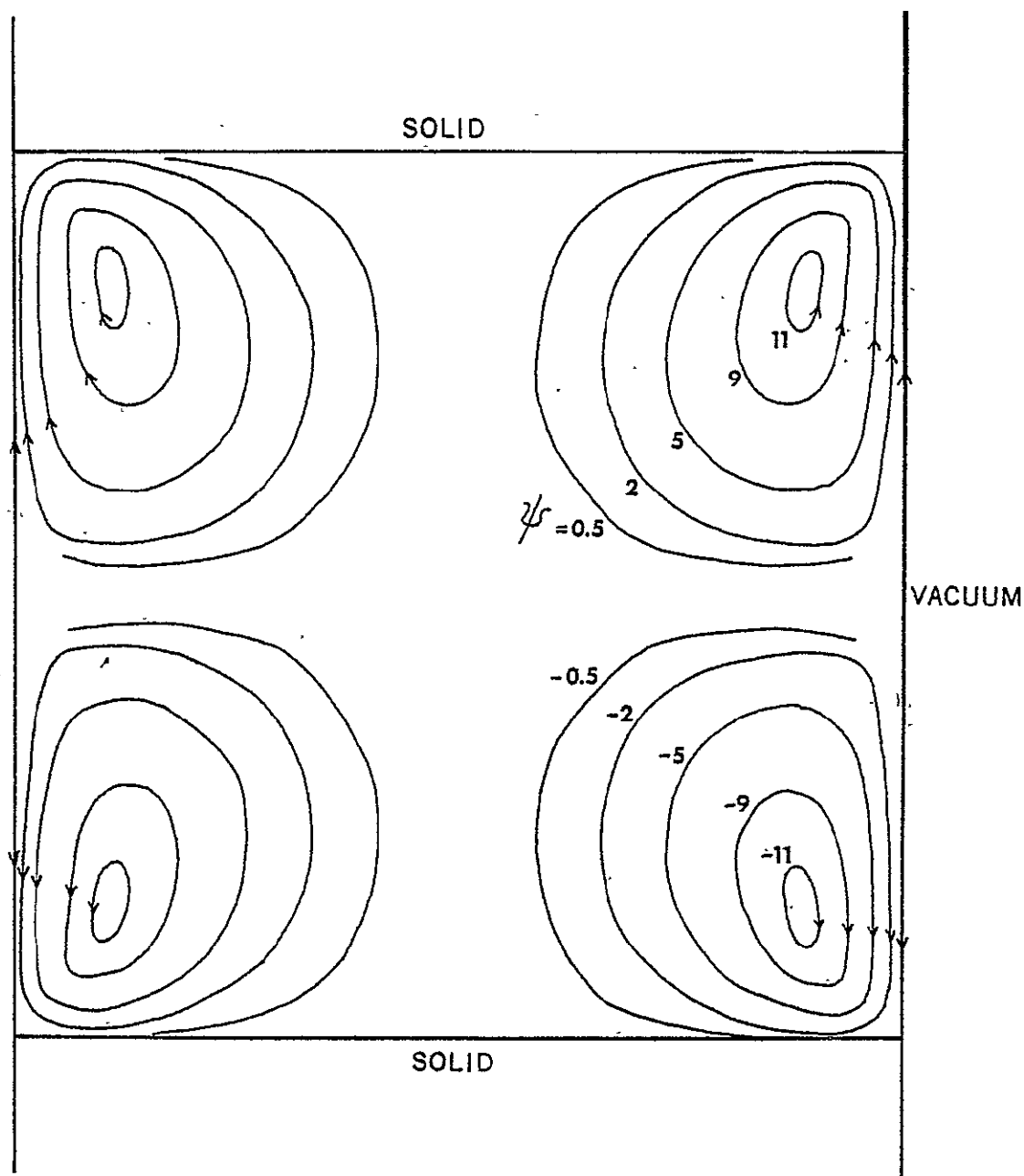


Figure 22. Computed dimensionless streamlines, ψ , for surface tension driven flow in floating zone melting of silicon at zero gravity, with a parabolic temperature profile on the free melt surface and $(T_0 - T_\infty) = 0.0125^\circ\text{C}$, $a = 2\text{ cm}$, $M' = 350$, and $v_c = 5\text{ cm/hr}$. Calculations performed with 11×21 grid.

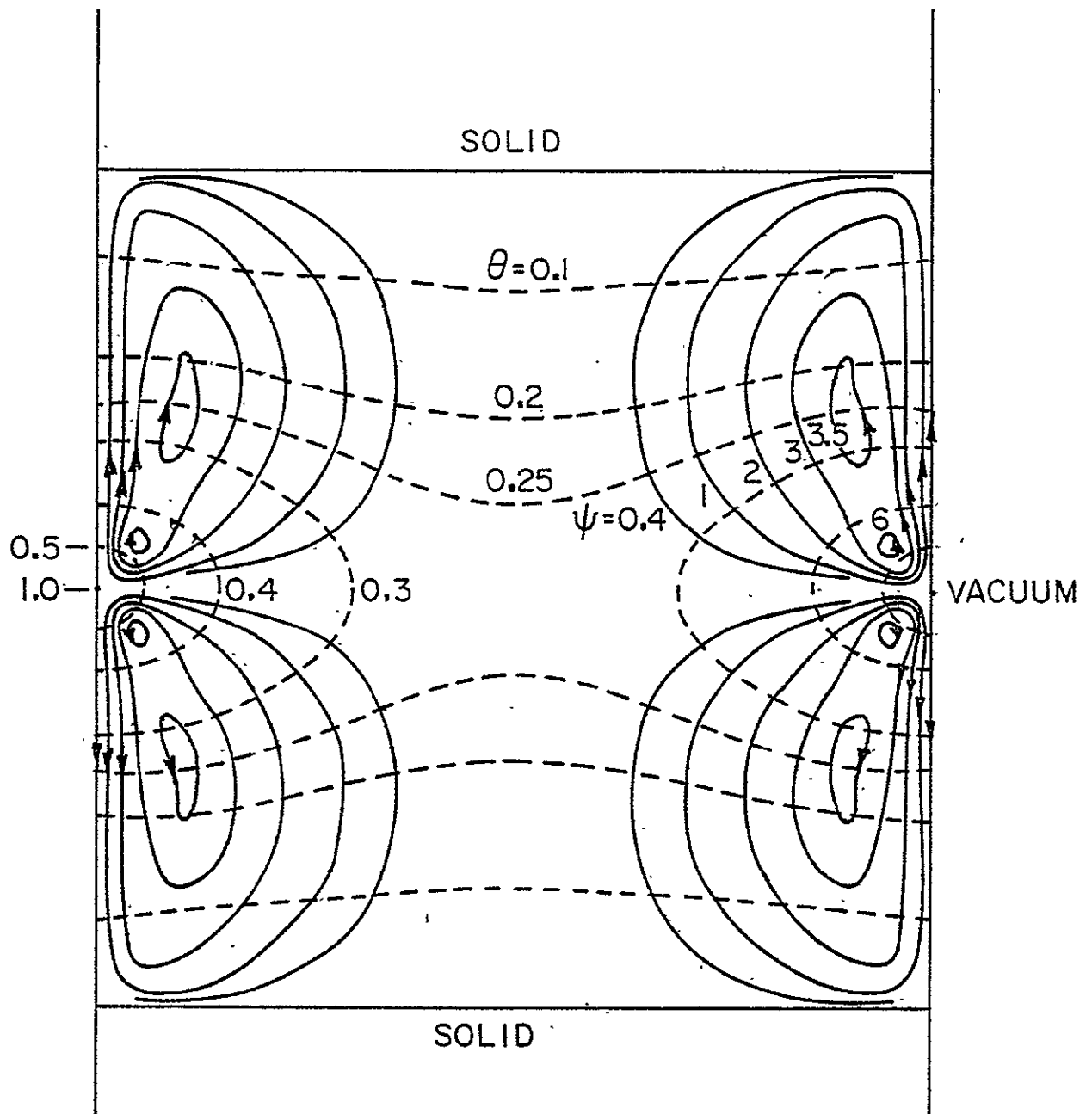


Figure 23. Computer calculated isotherms, θ , (dotted lines) and streamlines, ψ , (solid lines) for surface tension driven flow in floating zone melting at zero gravity, using the computed temperature fields for electron beam heating of silicon with $(T_o - T_m) = 0.0125^\circ\text{C}$, $T_c = T_m$, $\delta_s = 0.3$, $a = l = 2$ cm, $M' = 350$, $Pr = 0.023$, $v_c = 5$ cm/hr., and $\theta = (T - T_m) / (T_o - T_m)$. Calculations performed with 11×21 grid.

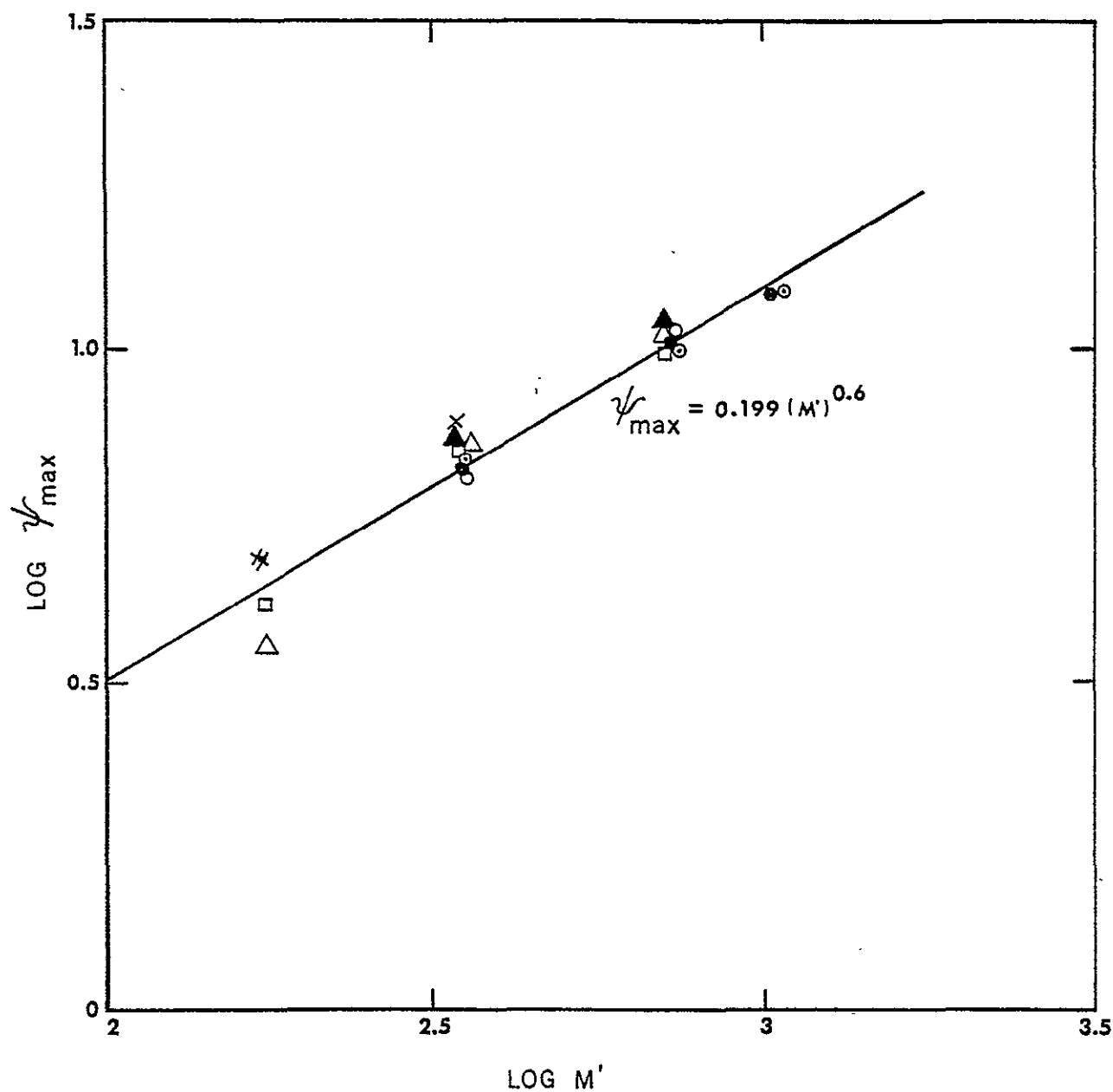


Figure 24. Correlation of the surface tension parameter, M' , and the maximum stream function, ψ_{\max} , of the surface tension driven flow in floating zone melting of silicon at zero gravity. The diameters of the zone in cm are: $D = 0.2$ (○), 1 (⊙), 2 (□), 4 (△), 8 (×), 10 (*).

The values of Γ are plotted as a function of Gr_h/M'^2 in Figure 25. As the value of Gr_h/M'^2 decreases, the buoyancy effect diminishes and the value of $\log \Gamma$ approaches zero. $1/M'$ and Gr_h/M'^2 are shown to be independent parameters defining the convection. This is also indicated by the momentum Equation (2) which contains both parameters, Gr_h/M'^2 and $1/M'$. No significant improvement was found when the values of Γ were plotted as a function of Gr_h/M' instead of Gr_h/M'^2 .

Finally, the buoyancy effect is represented in terms of the flow components in the zone in Figure 26. The axial flow velocity increases in the direction of gravity as the Grashof number increases. When the Grashof number is 6.2, the flow patterns approach those for pure surface tension driven flows.

V. FLOATING ZONE MELTING OF SAPPHIRE AT ZERO G

From the survey of the properties of materials of possible interest for space processing, sapphire was selected as the candidate material in view of its commercial importance and its unique transport properties, which are considerably different from silicon. The physical data surveyed for Al_2O_3 are substantially different from those estimated in the Annual Report [1]. The new data for Al_2O_3 , listed in this report, were used for the present study.

A. Computations with Free Parameters

The streamlines and the temperature profiles in the zone for electron beam heating were computed with free parameters chosen

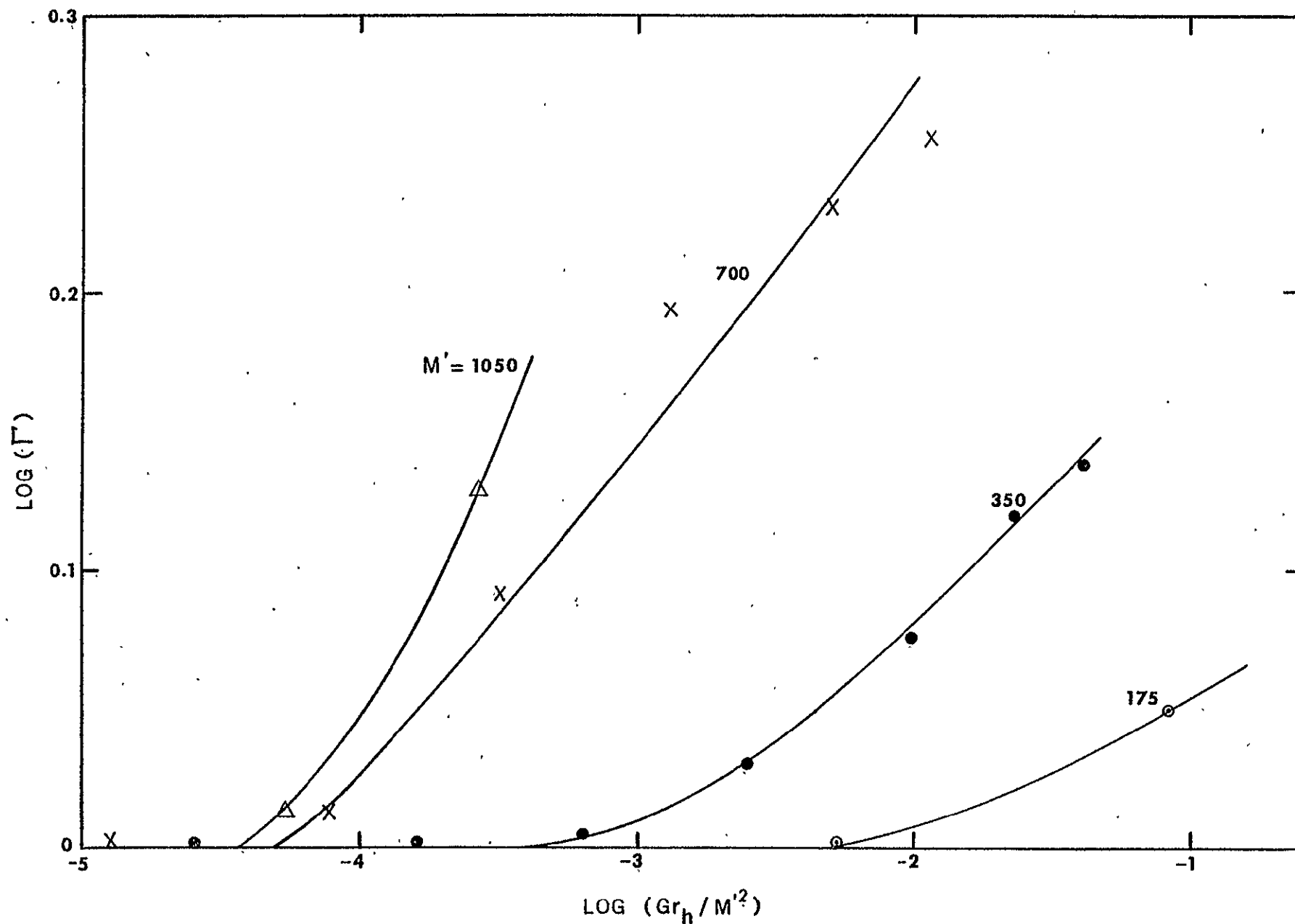


Figure 25. The ratio of Nusselt numbers, Γ defined by the equation (4), for the combined surface tension driven and buoyancy driven flow at 1 g to that for pure surface tension driven flow at zero g at the center of the freezing interface (bottom interface) versus Gr_h/M'^2 .

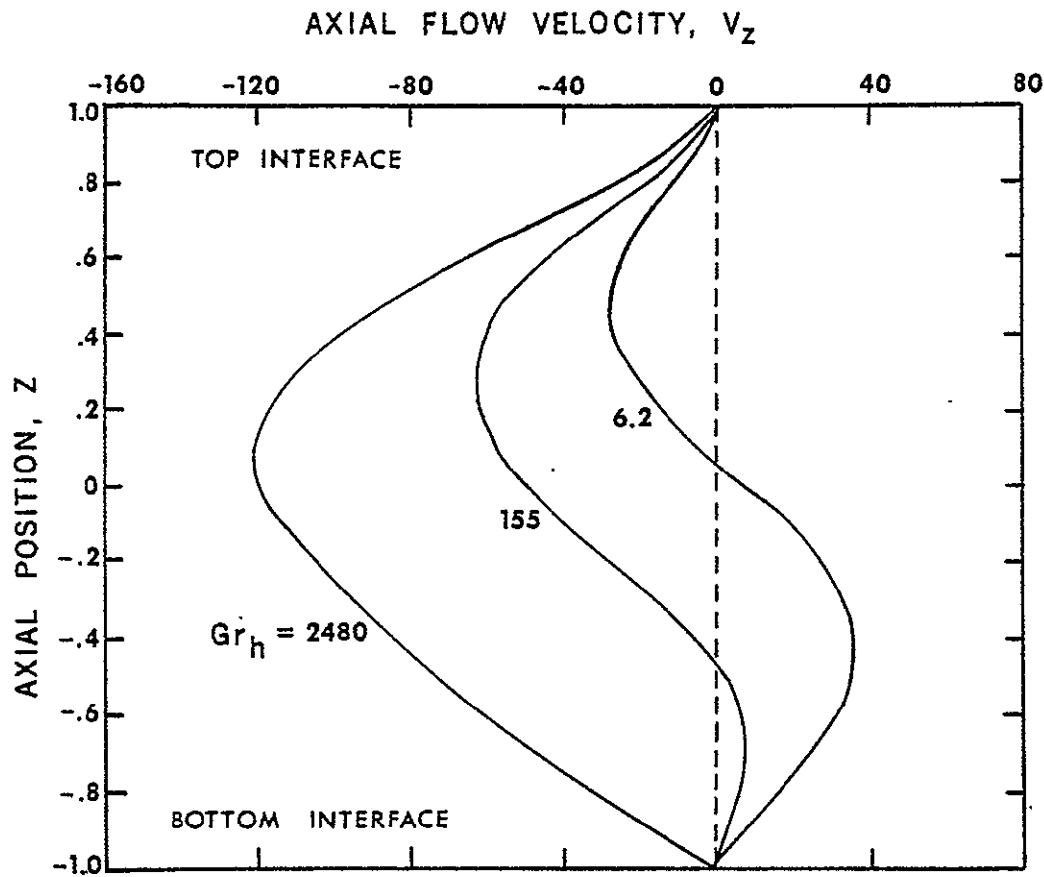


Figure 26. The influence of the Grashof number, Gr_h in the combined surface tension driven and buoyancy driven flow in the floating zone melting of silicon on the axial velocity component of flow, V_z along the center of zone for $M' = 700$. (- indicates the same direction as the gravity, and + the opposite).

from properties intermediate between those of silicon and sapphire, such as, $\mathcal{F} = 0.7$, $k = 0.024 \text{ cal/cm}^\circ\text{C}$, $C_p = 0.3 \text{ cal/g}^\circ\text{C}$, $\rho_f = 3.05 \text{ g/cm}^3$, $\mu = 2.72 \text{ CentiPoise}$, $\frac{\partial \gamma}{\partial T} = 0.06 \text{ dyne/cm}^\circ\text{C}$, $Pr = 0.34$, $(T_o - T_m) = 0.05^\circ\text{C}$, and $M' = 22$. The results are shown in Figure 27.

From the results studied so far with variable properties of materials we conclude that the intensity of the surface tension driven flow is primarily dependent upon the surface tension parameter M' , and the flow patterns change mainly as a result of variations in the Prandtl number.

B. Survey of the Physical Properties of Sapphire

Most of the sapphire melt physical properties required for the present study are available in the literature. The data employed are listed below:

- 1) Temperature coefficient of surface tension, $\partial\gamma/\partial T$, $0.465 \text{ dyne/cm}^\circ\text{C}$ [8].
- 2) Density, ρ , 3.05 g/cm^3
 3.66 g/cm^3 (solid).
- 3) Viscosity, μ , 0.6 g/cm sec [8].
- 4) Specific heat, C_p , $0.3 \text{ cal/g}^\circ\text{C}$ [9].
- 5) Thermal conductivity, k , $0.015 \text{ cal/cm}^\circ\text{C sec}$ [9].
- 6) Emissivity, ϵ_s , 0.5 [9].

Several potential problems are encountered in the floating zone melting of sapphire, particularly,

- 1) Suitability of electron beam heating, and
- 2) Effect of internal thermal radiation.

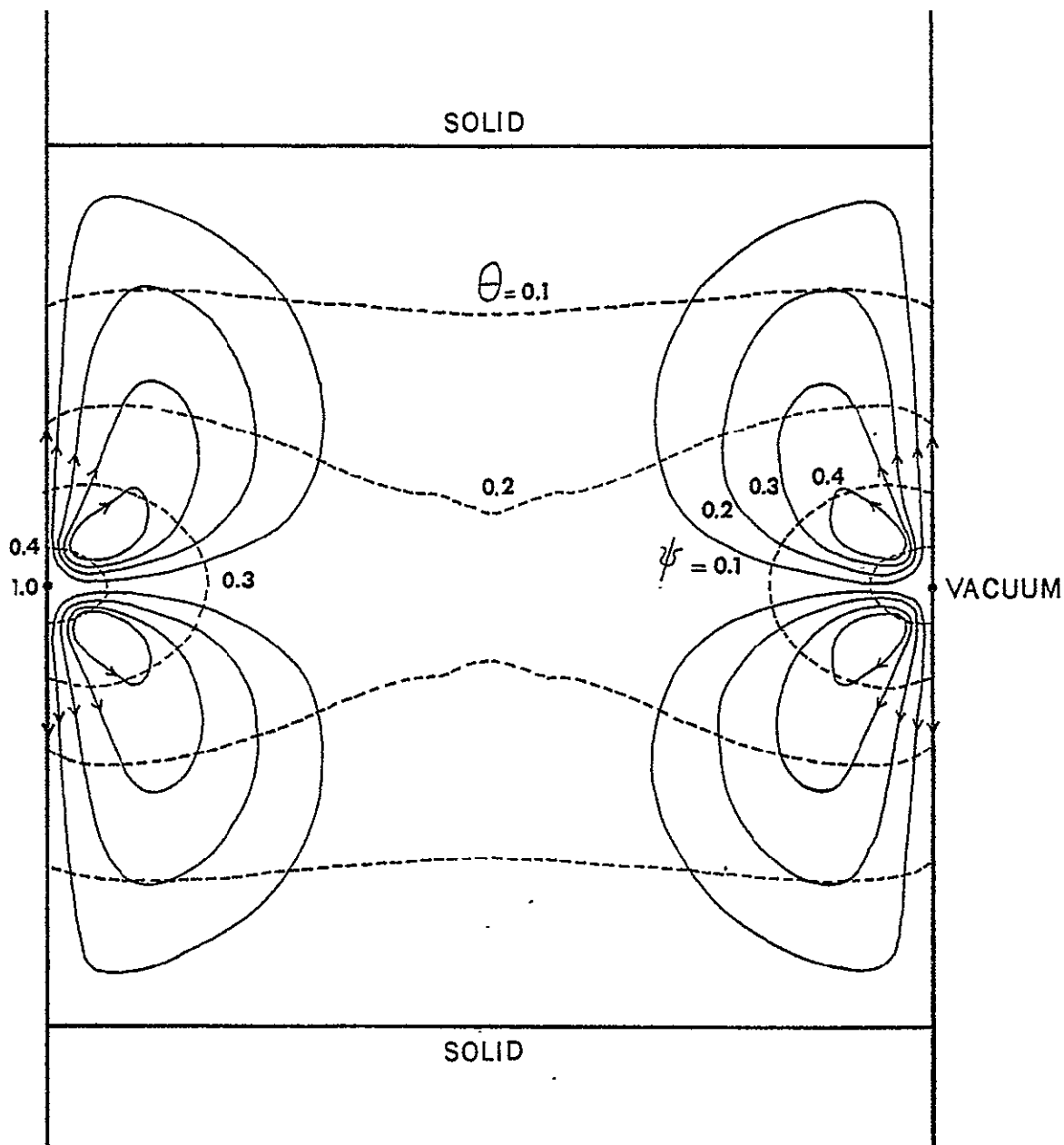


Figure 27. Computer calculated isotherms, θ , (dotted lines) and streamlines, ψ , (solid lines) for surface tension driven flow in floating zone melting at zero gravity, using the computed temperature fields for electron beam heating with free parameters such as: $(T_o - T_m) = 0.05^\circ\text{C}$, $T_c = T_m$, $\delta_s = 0.7$, $a = \ell = 0.5\text{ cm}$, $k = 0.024\text{ cal/cm}^\circ\text{C sec}$, $\rho_f = 3.05\text{ g/cm}^3$, $\mu = 2.72\text{ centipoise}$, $M' = 22$, $\text{Pr} = 0.34$, $v_c = 5\text{ cm/hr}$, and $\theta = (T - T_m)/(T_o - T_m)$. Calculations performed with 11×21 grid.

The electrical conductivity drastically increases from 10^{-2} to $15 \text{ ohm}^{-1} \text{ cm}^{-1}$ when Al_2O_3 is melted [10]. Therefore, electron beam heating may be feasible if the material is preheated to the melting point by other means. The infrared absorption of an Al_2O_3 melt is approximately 12 times that of the solid at melting point [11], which indicates that the radiation effect is relatively less important in the melt than in the solid. At present, it does not seem practical to rigorously include radiation in heat transfer calculations, due to the complexity of the problem. Therefore, approximate computations were made by using the apparent thermal conductivity, which takes the radiation heat transfer effect into account in terms of the conduction heat. Two modes of heating are considered in the following.

C. Computations with Electron Beam Heating

In order to determine the required heat shield temperature, T_c , for a given temperature of ring heat source, T_o , the temperature fields in the ingot were computed for various heat shield temperatures. For $(T_o - T_m) = 180^\circ\text{C}$ and 72°C , the required values of T_c to produce a zone of length equivalent to diameter were approximately 2033°C and 2010°C , respectively. The temperature profiles in the ingot are shown in Figures 28 and 29. From the physical data for sapphire, M' was estimated to be 35 with $(T_o - T_m) = 18^\circ\text{C}$, and 140 with $(T_o - T_m) = 72^\circ\text{C}$. The estimated Prandtl number is 12, and the radiation shape factor \mathcal{F} is 0.25 (see the following section).

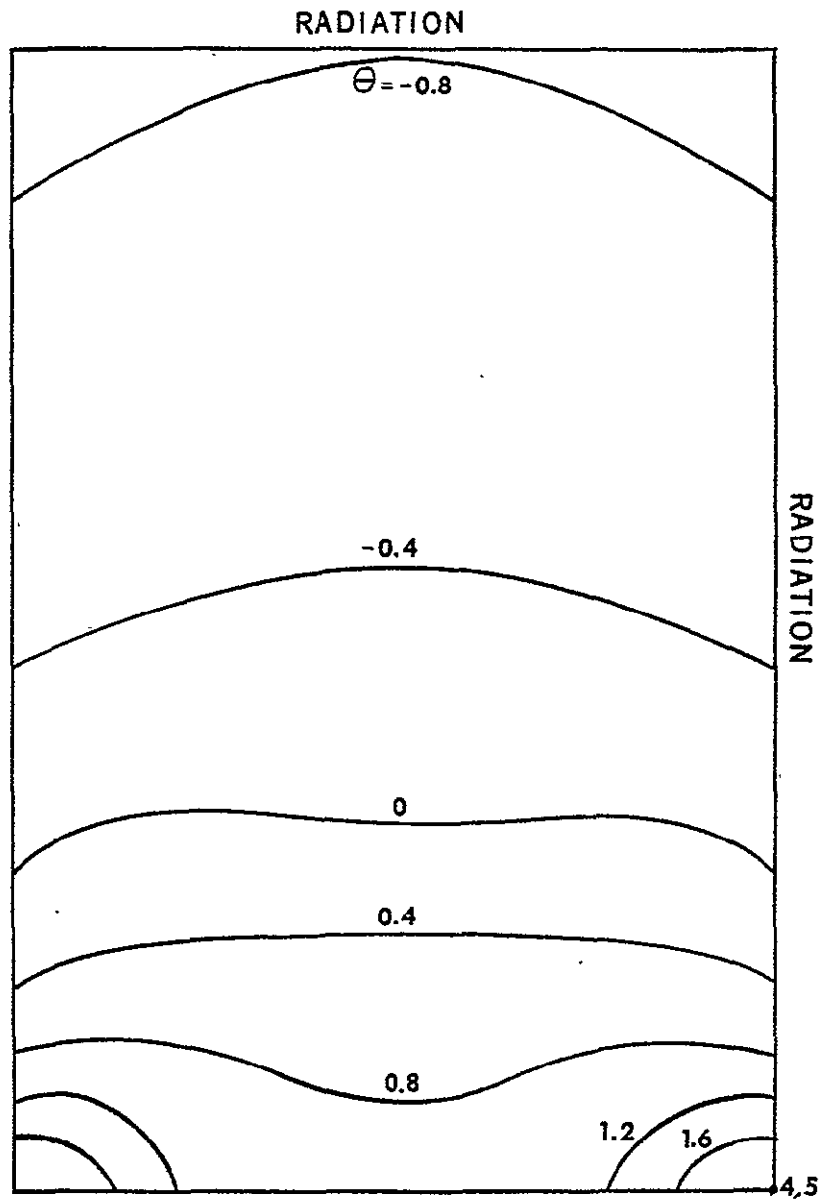


Figure 28. Computed isotherms, $\theta = (T - T_a) / (T_a - T_c)$, in the sapphire ingot above the center of the zone for electron beam heating, with $T_o = 2055^\circ\text{C}$, $T_c = 2033^\circ\text{C}$, $T_a = 2037^\circ\text{C}$, $a = 0.5\text{ cm}$, $f = 0.25$, and $k = 0.015\text{ cal/cm}^\circ\text{C sec}$. Thermal radiation boundary condition used at the end of the solid. Calculations performed with 11×31 grid.

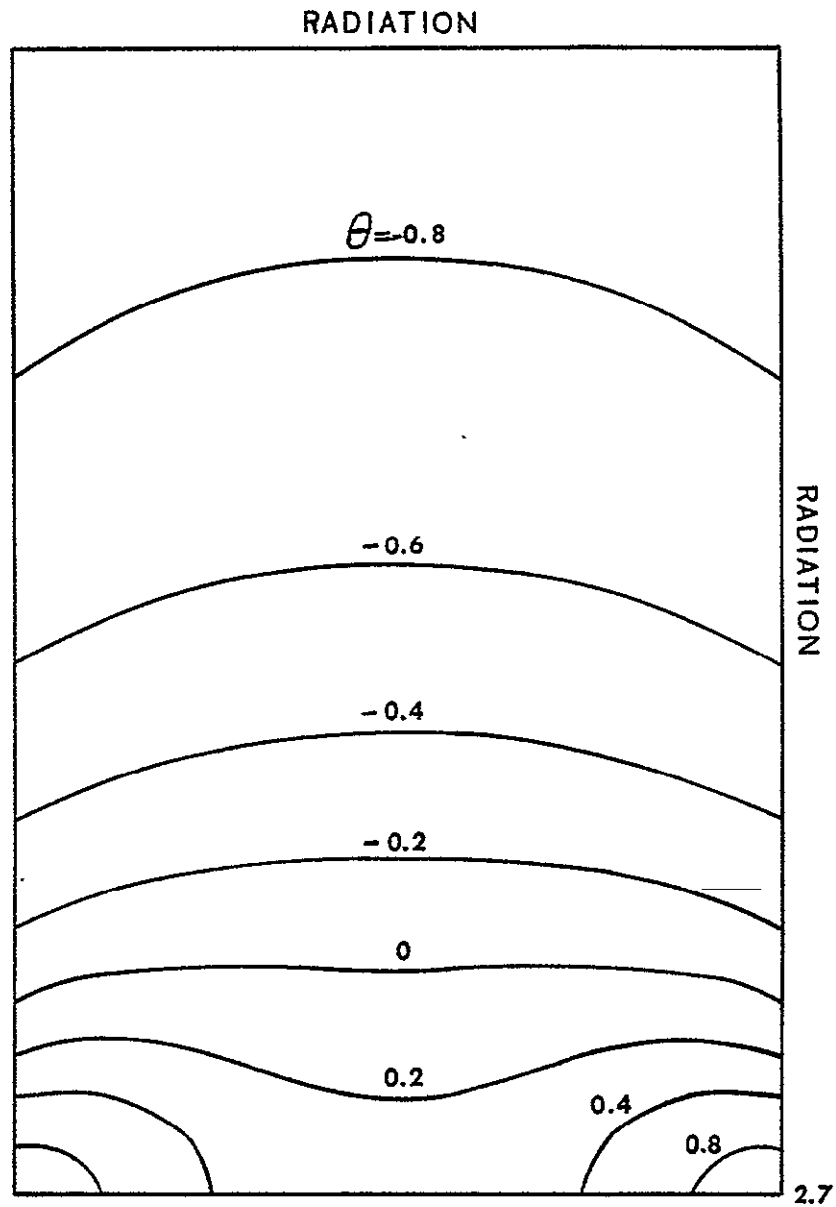


Figure 29. Computed isotherms, $\theta = (T - T_a) / (T_a - T_c)$, above the center of the zone in a sapphire ingot for electron beam heating, with $T_o = 2055^\circ\text{C}$, $T_c = 2033^\circ\text{C}$, $T_a = 2037^\circ\text{C}$, $a = 0.5\text{ cm}$, $f = 0.25$, and $k = 0.015\text{ cal/cm}^\circ\text{C sec}$. Thermal radiation boundary condition used at the end of the solid. Calculations performed with 11×31 grid.

In the zone of $a = \ell = 0.5$ cm the computed streamlines and temperature fields are shown in Figure 30 for $M' = 35$ and in Figure 31 for $M' = 140$. When $M' = 140$, the vortex near the ring heat source was larger compared with that in the silicon zone.

D. Computations with Radiation Heating

In order to simplify the problems of radiation heat transfer between the heater and the material, the following assumptions were made:

- 1) The heater temperature is uniform at T_h .
- 2) The radius of the heater approaches that of the zone.

The radiation shape factor, \mathcal{J} , between infinite parallel plates can be used under the condition of 2). For example, the heat flux between the heater and the zone, q , is

$$q = \sigma \mathcal{J} (T_h^4 - T^4) \quad (6)$$

where $\frac{1}{\mathcal{J}} = \frac{1}{\epsilon_s} + \frac{1}{\epsilon_h} - 1$ and ϵ_s and ϵ_h are the emissivity of the material in the zone and that of the heater, respectively, and σ is the Stefan-Boltzmann constant.

The emissivity [9] of metals of high melting point (for example, W, Mo, Ni, and Ta) is about 0.33 at $2600 \sim 2800^\circ\text{C}$ which is close to the required heater temperature for the floating zone melting of sapphire. With $\epsilon_h = 0.33$ and $\epsilon_s = 0.5$, the estimated \mathcal{J} from Equation (6) is 0.25.

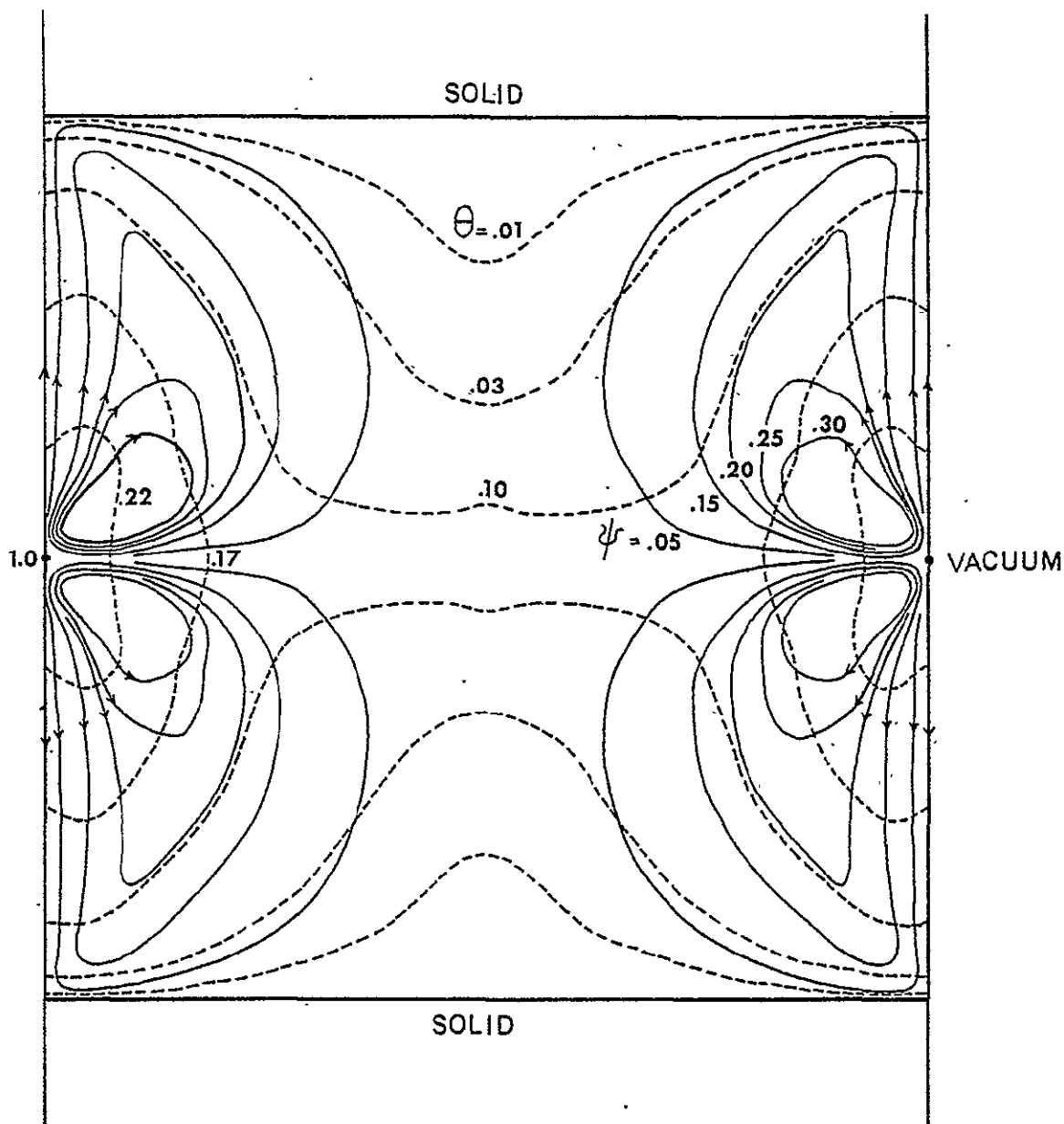


Figure 30. Computer calculated isotherms, θ , (dotted lines) and streamlines, ψ , (solid lines) for surface tension driven flow in floating zone melting at zero gravity, using the computed temperature fields for electron beam heating of sapphire, with $(T_o - T_m) = 18^\circ\text{C}$, $T_m = 2037^\circ\text{C}$, $T_c = 2033^\circ\text{C}$, $\mathcal{F} = 0.25$, $k = 0.015 \text{ cal/cm}^\circ\text{C sec}$, $a = \ell = 0.5 \text{ cm}$, $M' = 35$, $\text{Pr} = 12$, $v_c = 5 \text{ cm/hr.}$, and $\theta = (T - T_m) / (T_o - T_m)$. Calculations performed with 11×21 grid.

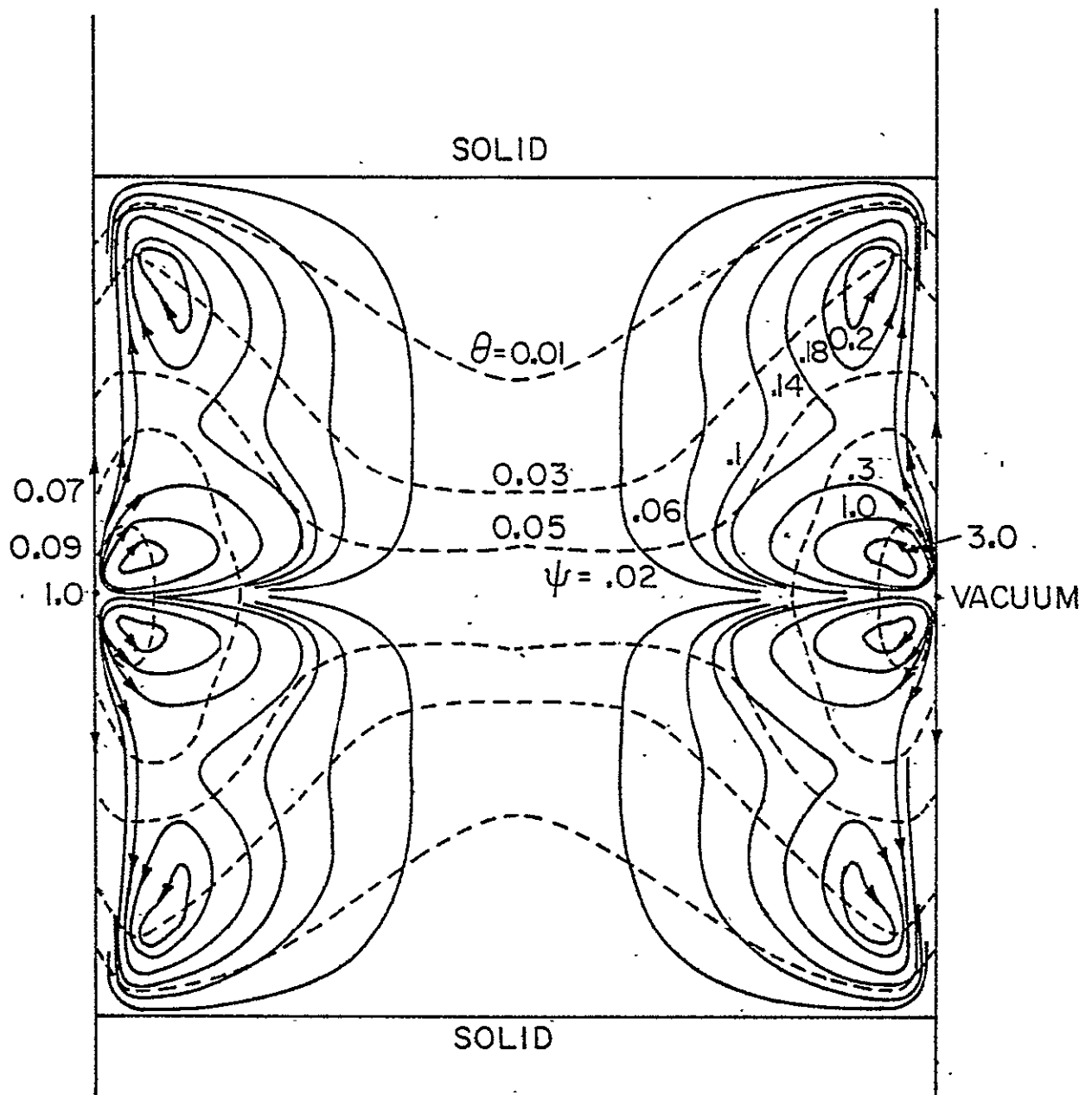


Figure 31. Computer calculated isotherms, θ , (dotted lines) and streamlines, ψ , (solid lines) for surface tension driven flow in floating zone melting at zero gravity, using the computed temperature fields for electron beam heating of sapphire, with $(T_o - T_n) = 72^\circ\text{C}$, $T_n = 2037^\circ\text{C}$, $T_c = 2010^\circ\text{C}$, $\mathcal{J} = 0.25$, $k = 0.015 \text{ cal/cm}^\circ\text{C sec}$, $a = \ell = 0.5 \text{ cm}$, $M' = 140$, $\text{Pr} = 12$, $v_c = 5 \text{ cm/hr.}$, and $\theta = (T - T_n) / (T_o - T_n)$. Calculations performed with 11×21 grid.

The temperature fields in the sapphire ingot without convection were computed for radiation heating and are plotted in Figure 32. The required heater temperature without convection was 2637°C. With the convection in the zone, however, the heater temperature can be lowered to 2337°C because of the more effective heat transfer to the convective zones.

With the radiation heater applied to sapphire floating zone melting, we were not able to obtain a steady state solution, since the temperature of the free melt surface did not reach a stable value. The temperature gradient near the center is reversed slightly with the increased number of iterations, which indicates that the flow might become oscillatory. Therefore, we feel that it is of interest to investigate the transient solutions for the floating zone melting of sapphire with a radiation heater.

E. Oscillatory Convection with Radiation Heating

Transient solutions are required to investigate the oscillatory flows in the floating zone melting of sapphire when thermal radiation heating is employed. The equations of momentum and heat transfer are developed for transient solutions as follows:

1) Equations for Transient Convection

The dimensionless momentum equation for pure surface tension driven flow is,

$$\frac{\partial \omega}{\partial \tau} + \frac{\partial(V_r \omega)}{\partial R} + \frac{\partial(V_z \omega)}{\partial Z} = \frac{\partial^2 \omega}{\partial Z^2} + \frac{\partial}{\partial R} \left\{ \frac{1}{R} \frac{\partial(R\omega)}{\partial R} \right\}. \quad (7)$$

The dimensionless heat transfer equation is,

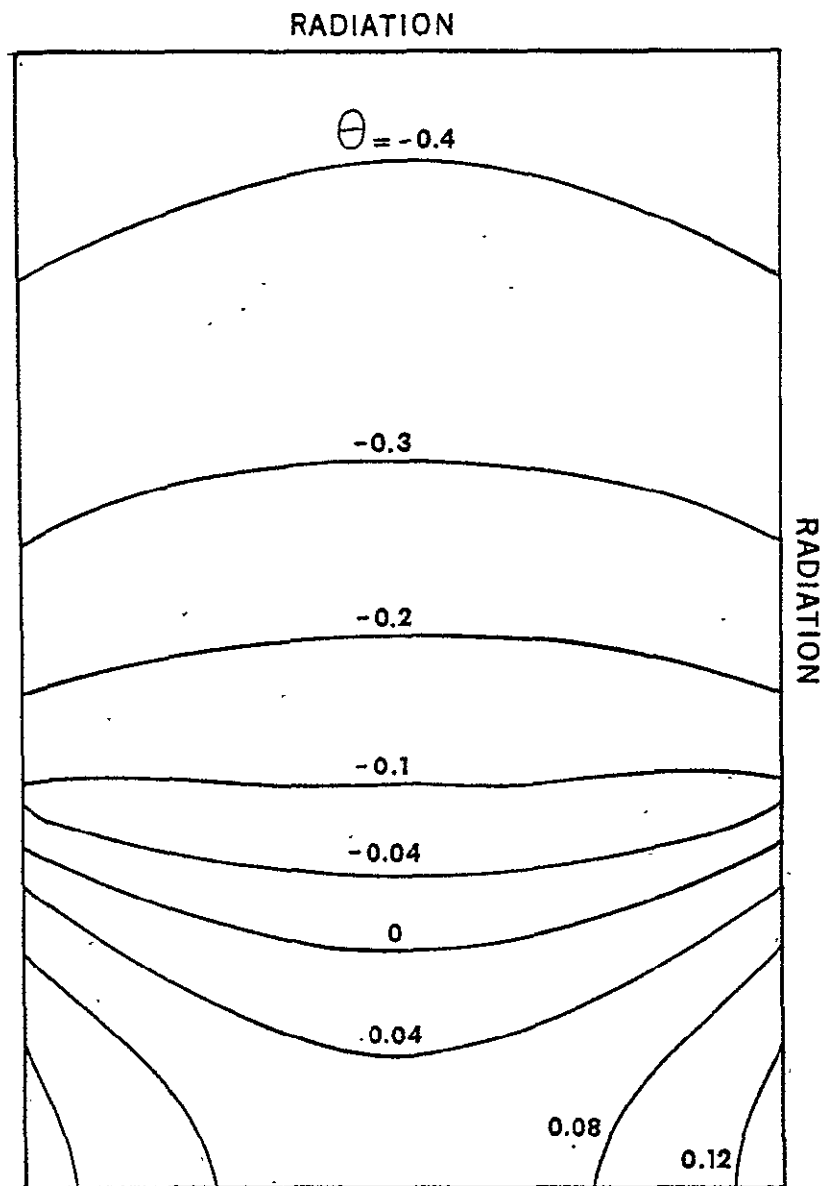


Figure 32. Computed isotherms, $\theta = (T - T_s) / (T_s - T_c)$ in the sapphire ingot above the center of zone for radiation heating with $T_h = 2637^\circ\text{C}$, $T_c = 23^\circ\text{C}$, $T_s = 2037^\circ\text{C}$, $a = 0.5\text{ cm}$, $\mathcal{J} = 0.5$ between the cooler and the ingot, and 0.25 between the heater and the ingot (uniform heater temperature assumed), and $k = 0.015\text{ cal/cm}^\circ\text{C sec}$. Thermal radiation boundary condition used at the end of the solid. Calculations performed with 11×31 grid.

$$\frac{\partial \theta}{\partial \tau} + V \frac{\partial \theta}{z \partial Z} + V \frac{\partial \theta}{r \partial R} = \frac{1}{Pr} \left\{ \frac{\partial^2 \theta}{\partial Z^2} + \frac{1}{R} \frac{\partial \theta}{\partial R} + \frac{\partial^2 \theta}{\partial R^2} \right\} \quad (8)$$

where, $\tau = \frac{vt}{a}$, $V_r = \frac{V_r a}{v}$, $V_z = \frac{V_z a}{v}$, and other parameters are defined as previously.

The approximate finite difference equations employed for the time dependent terms, $\partial \omega / \partial \tau$ and $\partial \theta / \partial \tau$ are:

$$\frac{\partial \omega}{\partial \tau} = \frac{\omega_{i,j}^* - \omega_{i,j}}{\Delta \tau} \quad (9)$$

$$\frac{\partial \theta}{\partial \tau} = \frac{\theta_{i,j}^* - \theta_{i,j}}{\Delta \tau} \quad (10)$$

Where $\Delta \tau = v \Delta t / a^2$ and the terms with the asterisk are the values at the end of time stem, $\Delta \tau$. The same numerical schemes as used in the steady state calculations are employed for the other terms in the equations.

2) Numerical Computations

The initial values for the stream function and the temperature were taken from one of the quasi steady state solutions. We were not able to obtain a converged solution with the time increment, both in the temperature and in the stream functions.

When the time dependent term was excluded from the momentum transfer equation (i.e., the transient condition is included only in the heat transfer calculation), the computer solutions were converged with a result that showed the oscillatory convection nature.

The calculation procedure used is as follows:

- 1) Initialization of the temperature field from the quasi steady state solution.
- 2) The stream function (based on steady state analysis) was computed using the initial temperature field from step 1).
- 3) The temperature field at the end of the first time increment of $\Delta\tau$ was computed using the flow field from step 2).
- 4) The stream function (based on steady state analysis) was computed using the temperature field from step 2).
- 5) Steps 3) and 4) were repeated.

As an illustration, the stream functions and temperature fields were calculated in the radiation heated floating zone melting of sapphire with the previously mentioned physical configurations and the time increment of $\Delta\tau = 0.0393$ (or $\Delta t = 0.05$ sec for sapphire). The results are shown in Figures 33 through 37 in sequence of the time interval of $2\Delta\tau$ for a period of approximately one oscillation cycle. The corresponding temperatures at the free melt surface are depicted in Figure 38. The convection cycle shown above was repeated with an extended time.

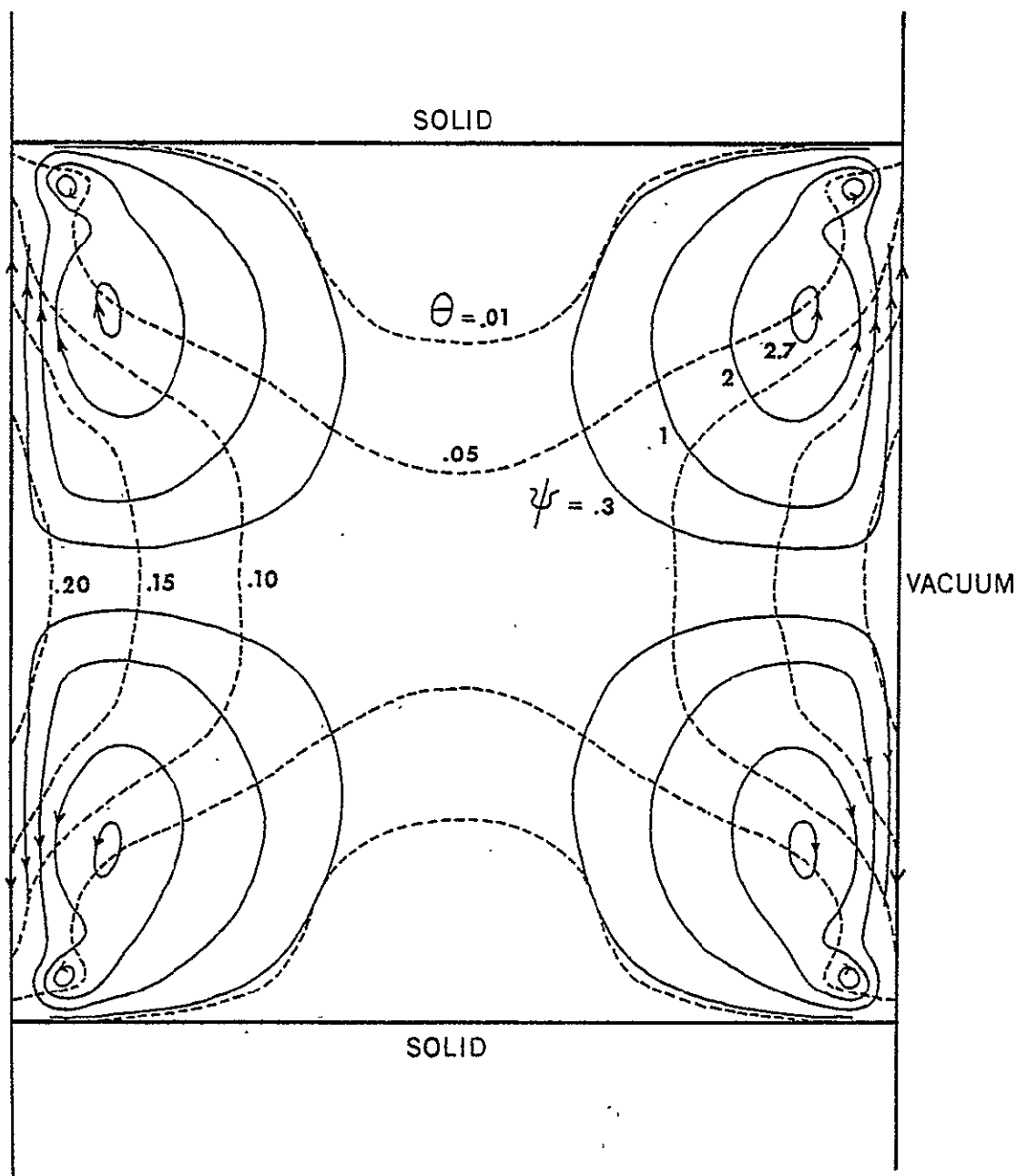


Figure 33. Computer calculated isotherms, θ , (dotted lines) and streamlines, ψ , (solid lines) for surface tension driven flow in floating zone melting at zero gravity, using computed temperature fields at $\tau=0$ for radiation heating of sapphire, with $(T_h - T_a) = 300^\circ\text{C}$, $T_a = 2037^\circ\text{C}$, $T_c = 23^\circ\text{C}$, $k = 0.015 \text{ cal/cm}^\circ\text{C sec}$, $\mathcal{J} = 0.25$, $a = l = 0.5 \text{ cm}$, $M' = 585$, $Pr = 12$, $V_c = 5 \text{ cm/hr}$, and $\theta = (T - T_a) / (T_h - T_a)$. Calculation performed with 11×21 grid.

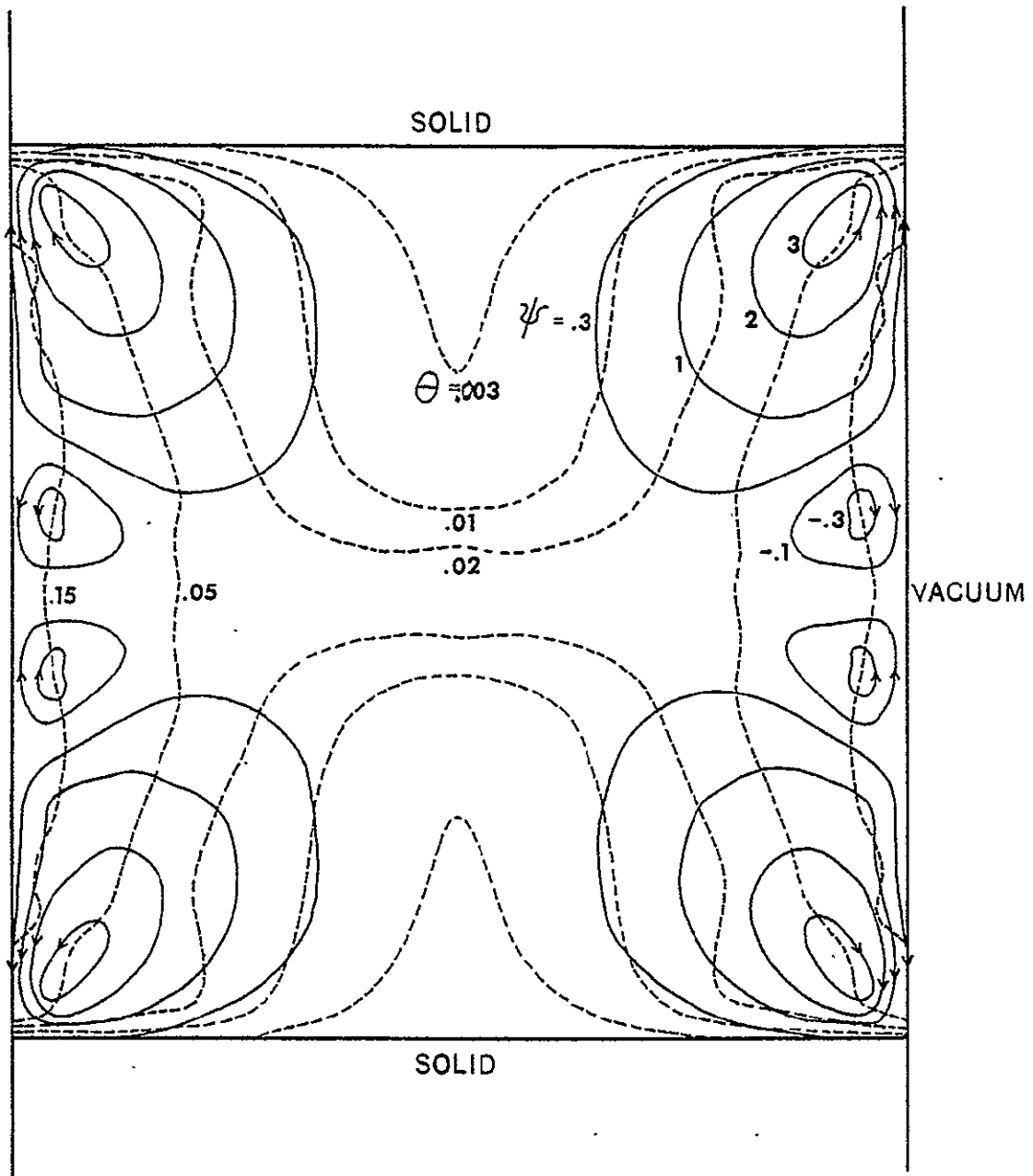


Figure 34. Same conditions as in Figure 33 except $\tau = 0.0786$.

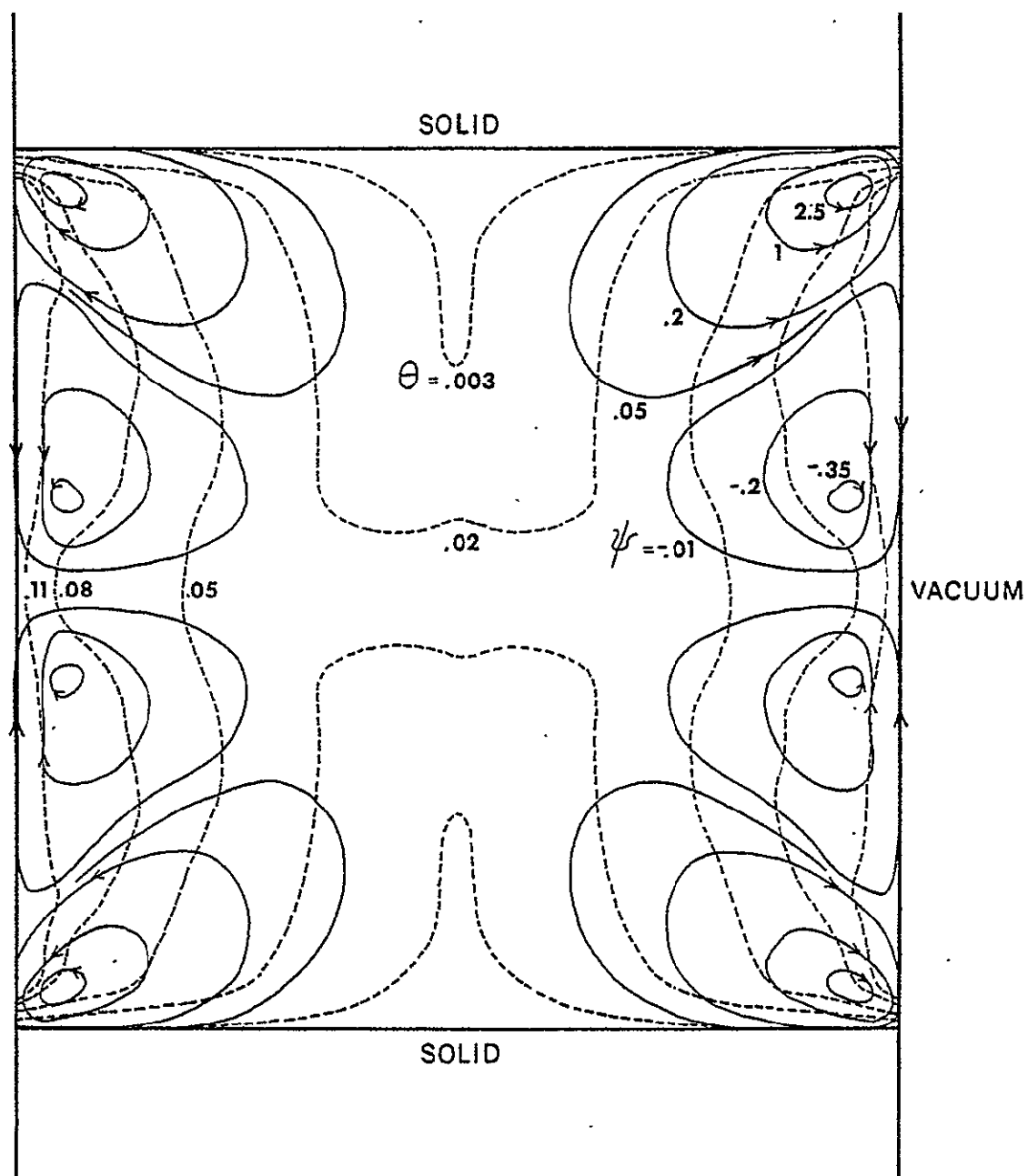


Figure 35. Same conditions as in Figure 33 except $\tau = 0.1572$.

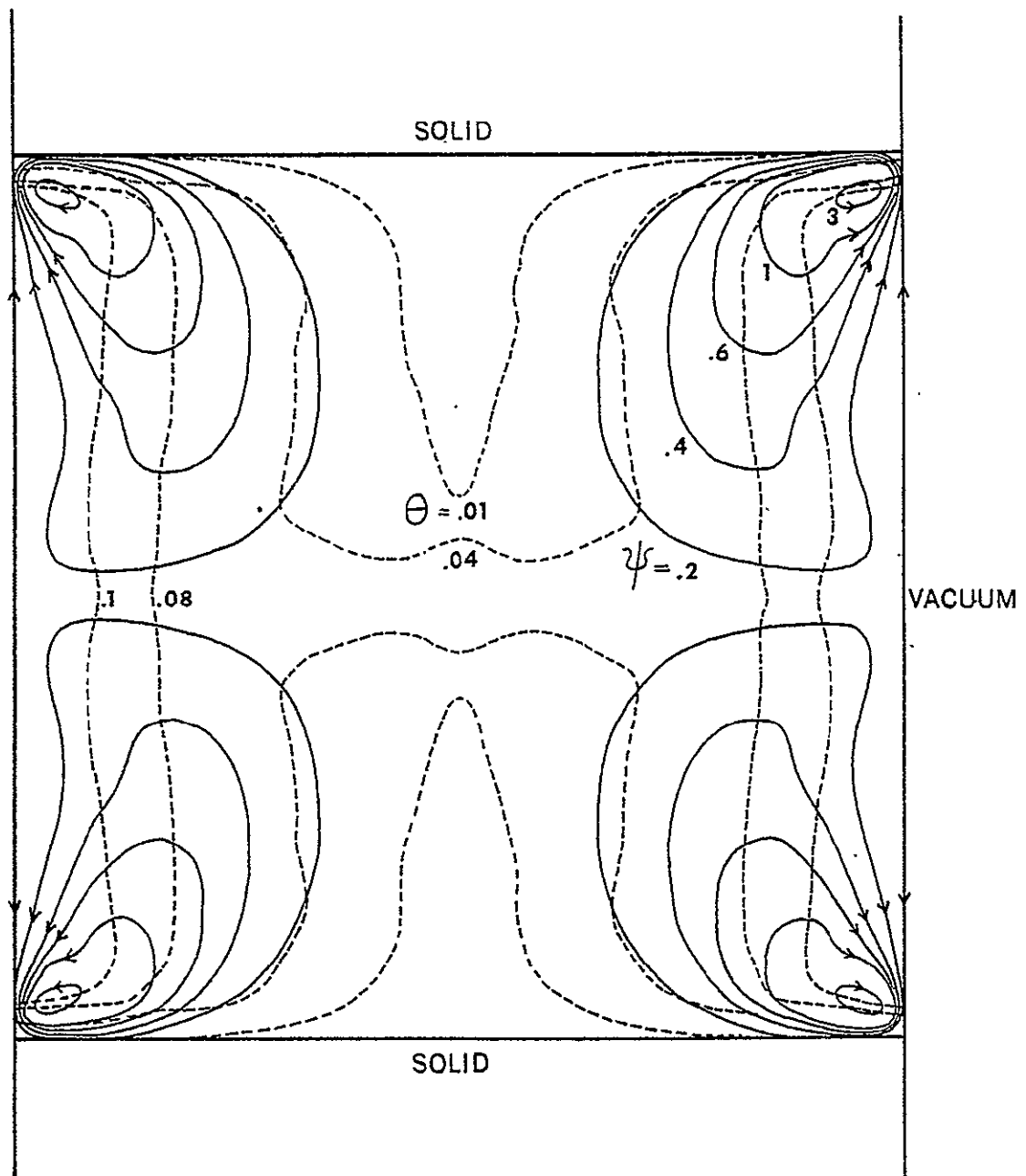


Figure 36. Same conditions as in Figure 33 except $\tau = 0.2358$.

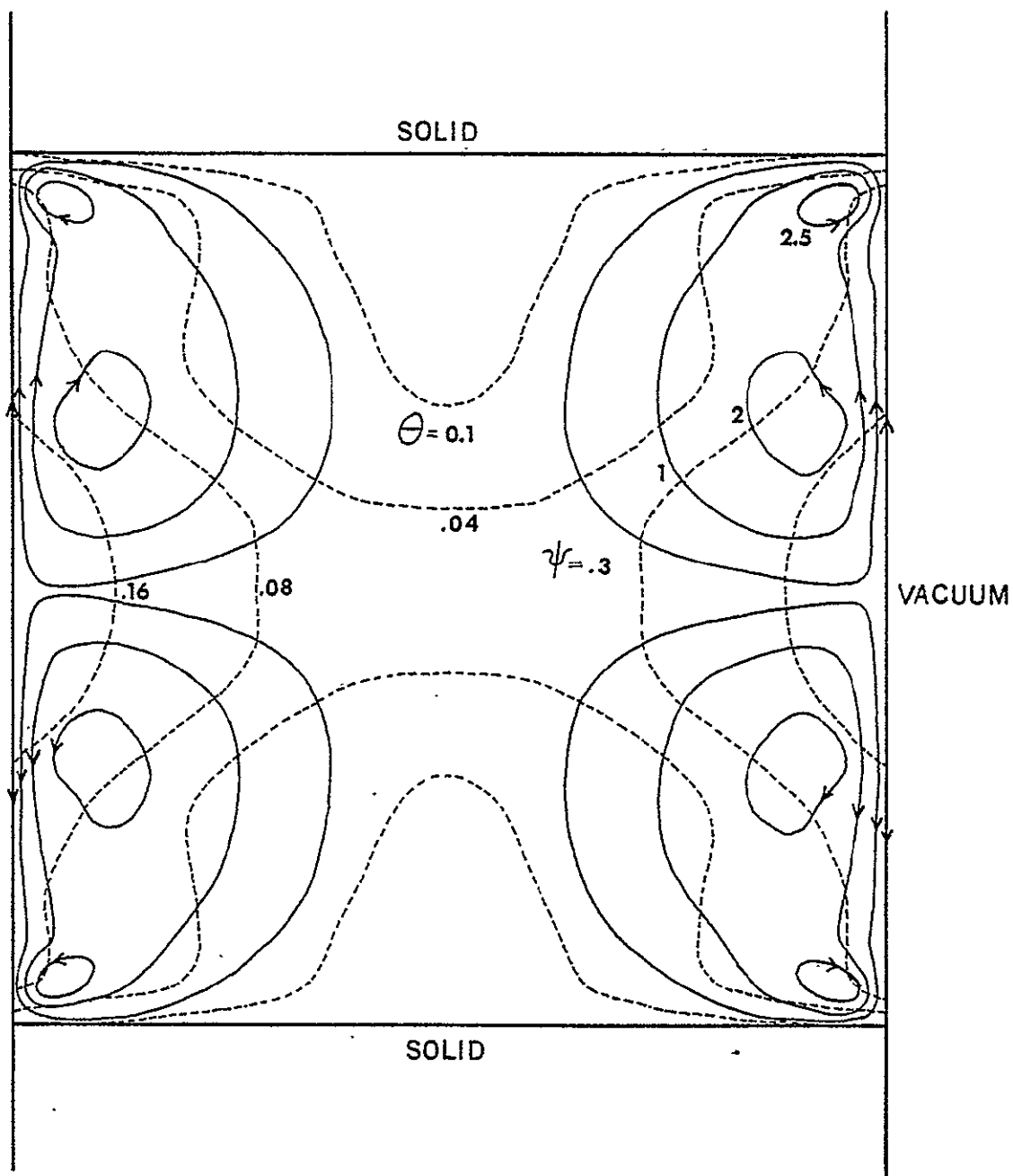


Figure 37. Same conditions as in Figure 33 except $\tau = 0.3144$.

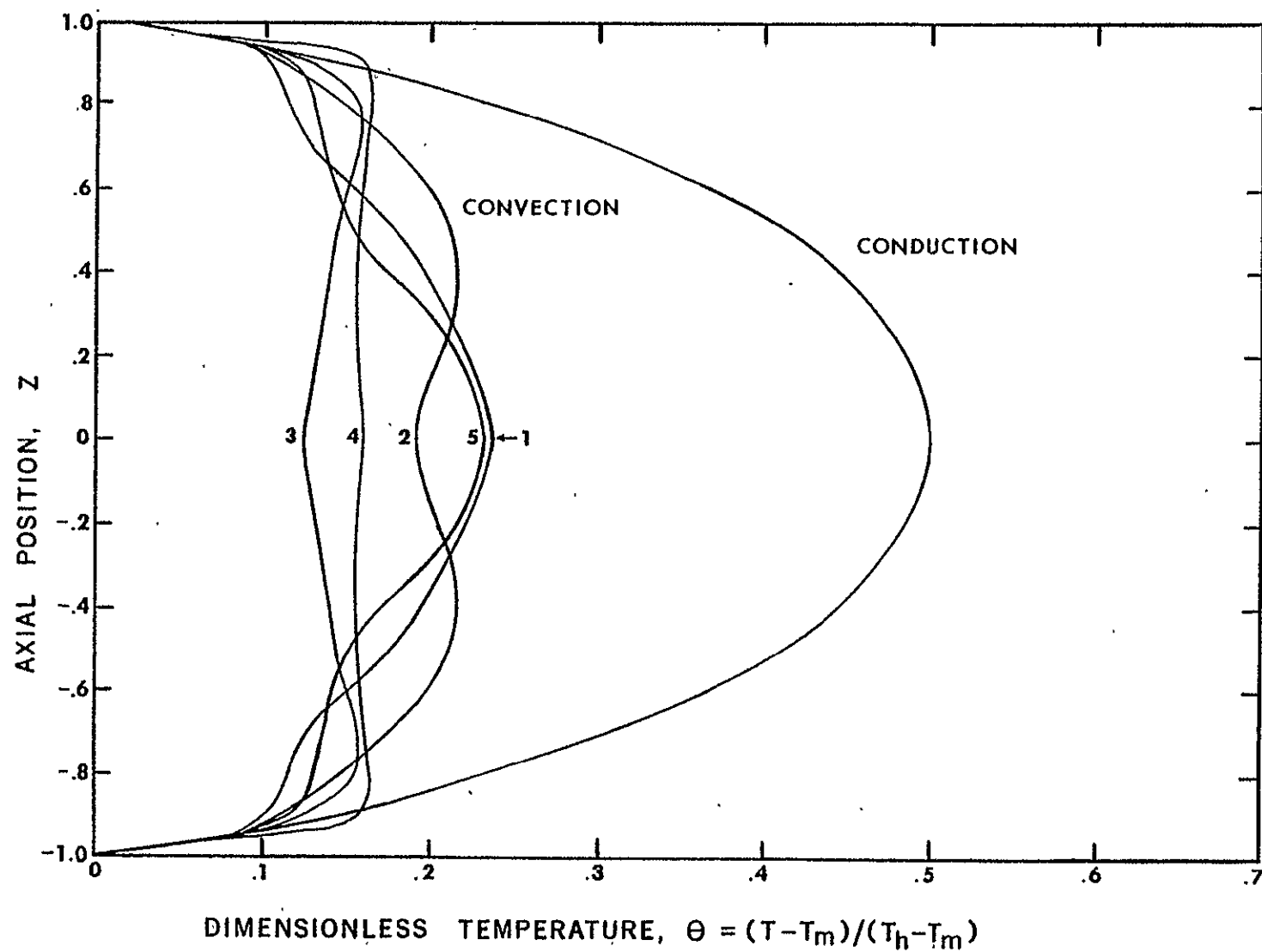


Figure 38. Temperature oscillation at the free melt surface. The numbers 1 through 5 indicate the temperature profiles corresponding to Figure 33 through 37, in sequence.

VI. PROPOSED ADDITIONAL STUDIES

The silicon calculations have demonstrated that surface tension driven convection can be significant even at the gravity of earth. Preliminary calculations on sapphire indicate that convection may be oscillatory when the molten zone is maintained by radiation heating. It is desirable to expand the studies on sapphire to further examine the question of oscillatory convection and to extend the analysis of surface driven convection to other systems of interest to space processing. Calculations of the type recently completed on InSb [12] and in progress on InSb-GaSb alloys [6, 13] should be expanded and extended to other solid solution systems of potential commercial value.

A number of experimental and theoretical studies have been conducted on various aspects of convection as related to space processing. The degree of interaction between investigators has not been optimum in all cases and all areas of conflict between theory and experiment have not been resolved. This would appear to be an excellent time to critically review the work that has been completed to date and determine the nature of future studies that should be conducted both to resolve conflicts and to maximize the benefits of previous investigations.

REFERENCES

- [1] "Analytics of Crystal Growth in Space," Annual Report for NASA, 5 June 1973 - 4 June 1974, Dept. of Chemical Engineering, University of Southern California.
- [2] C.E. Chang and W.R. Wilcox, J. Cryst. Growth 28, 8 (1975).
- [3] C.E. Chang and W.R. Wilcox, J. Cryst. Growth 28, 288 (1975).
- [4] V.F.S. Yip, C.E. Chang, and W.R. Wilcox, J. Cryst. Growth 29, 69 (1975).
- [5] C.E. Chang and W.R. Wilcox, Int. J. Heat and Mass Transfer, in press.
- [6] W.R. Wilcox and C.E. Chang, "Thermocapillary Convection in Floating Zone Melting," Third American Conference on Crystal Growth, Stanford, California, July 14, 1975.
- [7] R.A. Lefever, C.E. Chang, and W.R. Wilcox, "Surface Driven Convection in InSb-GaSb Melts Solidified Aboard Skylab III," American Physical Society, Pasadena, California, December 30, 1975.
- [8] Yu. V. Zubarev, et al., Inorganic Materials, Translated from Russian, 5, 1325 (1969).
- [9] Y.S. Touloukian, Ed., "Thermophysical Properties of Matter," Plenum, New York, 1973.
- [10] J.D. MacKenzie, Advances in Inorganic Chem. and Radiochem, 4, 293 (1962).
- [11] D.A. Grynak and D.E. Burch, J. Opt. Soc. Am. 55 (6), 625 (1965).
- [12] "Skylab M518 Multipurpose Furnace Convection Analysis," Final Report, Contract NAS8-27015, September 1975. Lockheed Missiles & Space Company, Inc., Huntsville, Alabama.
- [13] "Mixed III-V Crystal Growth in Very Low Accelerational Fields," Contract NAS8-28305, Monthly Progress Reports, 1975, R.A. Lefever, University of Southern California, Los Angeles, Calif.

APPENDIX A

DEFINITION OF SYMBOLS

a	Radius of the molten zone, cm
b	Distance of the top surface of the solid from the center of the zone, cm
C_p	Specific heat, cal/g°K
C	Dimensionless impurity concentration in the liquid, defined by m/m_t
C_{ct}	Dimensionless impurity concentration in the feed crystal, defined by m_{ct}/m_t
$C_{i,b}$	Dimensionless impurity concentration in the liquid at the crystallizing interface, defined by $m_{i,b}/m_t$
$C_{i,t}$	Dimensionless impurity concentration in the liquid at the melting interface, defined by $m_{i,t}/m_t$
D	Binary molecular diffusion coefficient, cm^2/sec
g	Acceleration, cm/sec^2
g_e	Earth's gravitational field, $980 \text{ cm}/\text{sec}^2$
Gr_h	Grashof number for heat transfer (\sim ratio of the temperature difference buoyancy force to the viscous force) defined by $g\beta(T_o - T_m)a^3/\nu^2$
Gr_m	Grashof number of mass transfer (\sim ratio of the composition buoyancy force to the viscous force) defined by $g\alpha m_t a^3/\nu^2$
i	Integer denoting grid station in axial direction, $i = 1, 2, 3, \dots$
j	Integer denoting grid station in radial direction, $j = 1, 2, 3, \dots$
k	Thermal conductivity, $\text{cal}/\text{cm sec}^\circ\text{C}$
k_o	Interfacial distribution coefficient (ratio of the impurity concentration in the crystal to that in the liquid at the interface)
l	One half of the liquid zone length, cm

m	Impurity concentration in liquid, g/cm^3
m_t	Impurity concentration the feed solid would have if it were melted, g/cm^3
m_{cb}	Impurity concentration in the crystal, g/cm^3
m_{ct}	Impurity concentration in the feed crystal, g/cm^3
$m_{i,b}$	Impurity concentration in the liquid at the crystallizing interface, g/cm^3
$m_{i,t}$	Impurity concentration in the liquid at the melting interface, g/cm^3
M'	Dimensionless surface tension parameter at the free liquid surface (\sim ratio of surface tension force to viscous force) defined by $\rho\sigma(T_o - T_m)a^3/\mu^2\ell^2$
Nu	Nusselt number (dimensionless temperature gradient, or ratio of total heat transport to heat conduction) defined by $ \partial\theta/\partial z _{\pm\ell}/a$
Nu_g	Nusselt number at the center of interface at the gravity of earth
Nu_0	Nusselt number at the center of interface at zero gravity
p	Dynamic pressure in fluid, dyne/cm^2 , $P - p_o$
p_o	Static pressure in fluid, dyne/cm^2 , defined by $\rho_f g(\ell - z)$
P	Total pressure in fluid, dyne/cm^2
Pr	Prandtl number, $\mu C_p/k$ (ratio of the momentum diffusivity to the thermal diffusivity)
r	Radial coordinate, measured from the center of the zone, cm
R	Dimensionless radial coordinate, measured from the center of the zone, r/a
ΔR	Dimensionless radial distance between grid points
Sc	Schmidt number (ratio of the momentum diffusivity to the molecular diffusion coefficient), $\mu/\rho D$

Sh	Sherwood number (dimensionless concentration gradient), defined by $ \partial C/\partial Z \pm \ell/a$
t	Time, sec
T	Temperature, °K
T _o	Temperature of the middle of liquid zone at the periphery, °K
T _c	Temperature of the surroundings, °K
T _m	Interfacial temperature (melting point), °K
T _h	Temperature of the heater, °K
T	Either (T _o - T _m) if θ is defined by the Equation, $\theta = (T - T_m)/(T_o - T_m)$, (T _m - T _c) if θ is defined by the Equation, $\theta = (T - T_m)/(T_m - T_c)$, or (T _h - T _m) if θ is defined by the Equation, $\theta = (T - T_m)/(T_h - T_m)$
v _c	Zone travel rate, cm/sec
v _o	Reference velocity, defined by $\sigma(T_o - T_m)a^2/\mu\ell^2$
v _z	Axial velocity component of the fluid, cm/sec
V _c	Dimensionless zone travel rate, v _c a/v
V _r	Dimensionless radial velocity component of the fluid, v _r a/v
V _z	Dimensionless axial velocity component of the fluid, v _z a/v
V _{cf}	Dimensionless interfacial flow rate, V _c (ρ _c /ρ _f)
z	Axial coordinate, measured from the center of the zone, cm
Z	Dimensionless axial coordinate, measured from the center of the zone, z/a
ΔZ	Dimensionless axial distance between grid points
α	(∂ρ/∂m) _{T, P} /ρ; volume expansion coefficient due to a concentration change in fluid, 1/(g/cm ³)
β	(∂ρ/∂T) _{m, P} /ρ; volume expansion coefficient due to a temperature change in fluid, 1/°C

γ	Surface tension between melt and vapor, dyne/cm
Γ	Ratio of the Nusselt numbers for combined surface tension driven and buoyancy driven convection, defined by Nu_g/Nu_o
ϵ_s	Emissivity of thermal radiation
\mathcal{J}	Geometry factor for radiation heat transfer
θ	Dimensionless temperature, $(T-T_m)/\Delta T$
θ_c	Dimensionless temperature of the surroundings, $(T_c - T_m)/\Delta T$
μ	Viscosity of the fluid, g/cm sec
ν	Kinematic viscosity, μ/ρ , cm^2/sec
ρ	Density of the fluid, g/cm^3
ρ_c	Density of the crystal, g/cm^3
ρ_f	Density of the fluid at melting point, g/cm^3
σ	Stefan-Boltzmann constant, $5.668 \times 10^{-5} \text{ erg}/\text{cm}^2 \text{ sec } ^\circ\text{K}^4$
σ	Temperature coefficient of the surface tension, $\partial\gamma/\partial T$, dynes/cm $^\circ\text{K}$
τ	Dimensionless time defined by $\nu t/a^2$
ψ	Dimensionless stream function, defined by $V_r = \frac{1}{R} \frac{\partial \psi}{\partial Z}$ and $V_z = -\frac{1}{R} \frac{\partial \psi}{\partial R}$
ψ_{max}	Dimensionless maximum stream function in the zone for pure surface tension driven flow
ω	Dimensionless vorticity, defined by $\omega = \frac{1}{R} \left(\frac{\partial^2 \psi}{\partial R^2} - \frac{1}{R} \frac{\partial \psi}{\partial R} + \frac{\partial^2 \psi}{\partial Z^2} \right)$